

The Effect of Bridge Abutment Length on the Turbulence Structure and the Flow Through the Opening

Ken Vui Chua¹, Bruño Fraga², Thorsten Stoesser, M. ASCE³, Terry Sturm, F. ASCE⁴, and Seung Ho Hong⁵

¹Hydro-environmental Research Centre, School of Engineering, Cardiff University, The Parade, Cardiff, UK CF24 3AA. Email: chuakv@cardiff.ac.uk

²School of Engineering, University of Birmingham, Edgbaston, Birmingham, UK B15 2TT. Email: B.Fraga@bham.ac.uk

³Engineering Fluid Dynamics Research Centre, School of Civil, Environmental and Geomatic Engineering, University College London, Gower Street, London, UK WC1E 6BT. Email: t.stoesser@ucl.ac.uk

⁵Department of Civil and Environmental Engineering, West Virginia University, Morgantown, WV, US 26506. E-mail: sehong@mail.wvu.edu

⁴School of Civil and Environmental Engineering, Georgia Institute of Technology, Atlanta, GA, US 30332. E-mail: terry.sturm@ce.gatech.edu

ABSTRACT

The method of large eddy simulation (LES) is employed to investigate the flow and the turbulence structure around bridge abutments of different lengths placed in a compound, asymmetric channel. The simulations are faithful representations of large-scale physical model experiments which were conducted in the hydraulics laboratory at the Georgia Institute of Technology. The experiments are considered idealised hydraulic models of the Towaliga River bridge at Macon, Georgia, USA, consisting of flat horizontal floodplains on both sides of a parabolic main channel, two spill-through abutments with varying lengths (long-set back, LSB and short-set back, SSB)

24 and a bridge spanning across the abutments. In the LES a 'free flow' scenario is simulated where
25 the water surface is not perturbed by the bridge at any point. The Reynolds number, based on
26 the bulk velocity and hydraulic radius are 76,300 and 96,500 for LSB and SSB abutments re-
27 spectively. Validation of the simulation results using data from the complementary experiment is
28 presented and agreement is found to be reasonably good. Thorough comparison of various flow
29 variables between LSB and SSB scenarios to highlight the effect of the flow contraction is carried
30 out in terms of flow separation and instantaneous secondary flow, streamwise velocity, streamlines,
31 streamtraces and turbulence structures. Further flow instability and vortex shedding generated in
32 the shear layer downstream of the abutments are quantified by analysing timeseries of the instan-
33 taneous velocity in the form of probability density function, quadrant analysis and power density
34 spectra.

35 **INTRODUCTION**

36 Bridge support structures cause flow contraction and the formation of scour around the bridge
37 foundation that, according to the literature, may lead to bridge failure. During extreme flood events,
38 the scale of the scouring process is magnified, leading to higher chance of bridge failure. Shirole
39 and Holt (1991) collected data on about 1000 bridges for 30 years since the sixties and reported
40 up to 60% of the bridge failures were due to scour at the bridge foundation. Data collected for
41 the following 12 years on over 500 bridges has a similar outcome of 53% failure due to flood and
42 scour (Wardhana and Hadipriono 2003). More recently, Lin et al. (2014) carried out a very detailed
43 study on the scour type, scour depth and flow characteristics in 36 historically failed bridges. It
44 was concluded that 64% of the bridge failures were caused by local scour. However, the accurate
45 prediction of scour has always been a challenge for researchers and engineers.

46 Experimental work on scour formation around abutment-like structures has generally concen-
47 trated on deducing scour-prediction formulas by defining a few of the key parameters affecting
48 scour such as the abutment length, flow depth, abutment shape, flow intensity and sediment charac-
49 teristics(Melville 1992; Melville 1995). Laursen (1963) suggested that local abutment scour could
50 be predicted as an amplification factor applied to a theoretical contraction scour depth. However,

51 later studies modified Laursen's approach and proposed that the amplification factor for abutment
52 scour in compound channels should be applied on the basis of a discharge contraction ratio rather
53 than a geometric contraction ratio (Sturm and Janjua 1994; Sturm 2006; Ettema et al. 2010). Hong
54 et al. (2015) investigated three different water depths, including free surface, submerged orifice
55 and overtopping flows, with the inclusion of a bridge structure and found that turbulent kinetic
56 energy (TKE) near the bed could be related to the amplification factor used for scour prediction as
57 regions of high TKE coincide with the scour location. Scour-prediction formulas are very useful to
58 practical forecasting of the erosion around in-stream structures but they do not provide detailed un-
59 derstanding of the physical processes involved, especially as related to turbulence, flow separation,
60 and flow contraction combined.

61 The scouring mechanism around large obstacles is well documented. Large-scale energetic
62 coherent structures are induced by the presence of immersed bodies that contribute and magnify
63 the shear stress and pressure fluctuations originating at the channel bed. As a result, solid particles
64 are detached and entrained from the bottom sediment layer and a scour hole begins developing
65 around the in-stream structure (Sumer and Fredsøe 2002; Fael et al. 2006). Koken and Constan-
66 tinescu (2014) described the scour process around abutment-like structures in three main steps:
67 (1) the acceleration of flow past the flank or edge of the abutment; (2) the horseshoe vortex (HV)
68 structure forming because of the downflow and adverse pressure gradients present in the vicinity of
69 the upstream side of the abutment; and (3) the vortical structures shed in the separated shear layer
70 (SSL) forming in between the fast outer flow and the recirculation region behind the abutment.
71 Koken and Constantinescu (2014) used detached eddy simulation (DES) to simulate a trapezoidal
72 abutment with sloped sidewalls in a straight channel and found that when compared to simple ver-
73 tical spur dikes/abutments (Paik and Sotiropoulos 2005; Koken and Constantinescu 2008b; Koken
74 and Constantinescu 2008a; Koken 2011), the formation, dynamics and position of the large-scale
75 coherent structures around the abutment are very different, mainly due to the reduced deceleration
76 and smaller adverse pressure gradient of the incoming flow on the upstream face of the abutment.
77 (Koken 2017) continued his previous work and added another spill-through abutment on the other

78 side of the channel to obtain insights on the generation of coherent structures in the contraction.
79 A number of studies investigated the hydraulics of one-sided compound channels and generally
80 reported a particular interest at the interface between the main channel and floodplain, where the
81 secondary flow drives the lateral momentum transfer between the main channel and the floodplains,
82 increasing the bed stress on them (Cater and Williams 2008; Kara et al. 2012; Xie et al. 2013).

83 Most of the aforementioned numerical studies that involve a free surface and large obstructions
84 to the flow employed the so called rigid-lid assumption, in which a fixed (generally flat) surface or
85 lid is used to represent the water surface. In the majority of the cases, the validity of the assumption
86 can be justified by a low Froude number (i.e. $Fr < 0.5$) (see (Rodi et al. 2013) for more discussion).
87 Kara et al. (2015) performed LES to compare two different treatments of the free surface in a
88 channel with side mounted abutment: rigid-lid and level-set method (LSM). They showed that the
89 turbulence structure in the flow is strongly influenced by the water-surface deformation while high-
90 lighting the limitation of the rigid lid approximation and the requirement for more sophisticated
91 approaches. Yue et al. (2005) carried out LES on turbulent flow of different flow depths over a fixed
92 two-dimensional dune in which the free surface is computed using the LSM. The results suggested
93 strong interaction between the free surface and near-bed flow structures in the shallower flow case,
94 providing insights that the use of moving and deforming free surface is necessary especially in
95 relative shallow water.

96 This study attempts to contribute to the design of resilient hydraulic structures by elucidating
97 the complex flow mechanisms around bridge abutments in changing conditions. Large eddy sim-
98 ulations of the turbulent flow around bridge abutments of different lengths are performed, using
99 the level-set method to predict the free surface deformation. The relatively high constriction to
100 which the flow is subjected may produce fairly high local Froude numbers that prevent the rigid lid
101 assumption. The simulations are an exact reproduction of the large-scale laboratory experiments
102 of Hong et al. Hong et al. (2015) the data of which are used to validate the simulations. The com-
103 putational domain consists of an asymmetrical compound geometry with a parabolic main channel
104 in which two variable-length abutments with sloped sidewalls and rounded corners are placed. The

105 challenge of the present study from a numerical point of view relies on the concurrence of several
106 factors: a) a numerical setup that solves the larger scales of turbulence; b) fluid-structure inter-
107 action, including important flow contraction; c) free-surface prediction; d) complex and realistic
108 (compound and asymmetric) channel. To the authors' knowledge, such analysis has rarely been
109 carried out in the past, less so with these factors combined. The present paper proceeds firstly to
110 validate the large-eddy simulation with complementary experimental data. It then discusses the
111 differences on the mean flow patterns between the two abutment configurations, focusing on the
112 effect of increasing contraction on the extent of the recirculation vortices and the oscillation of the
113 shear layer between this recirculation and the main channel flow. Thirdly, the results focus on the
114 analysis of the coherent structures shed by the abutments, whose shapes, vorticity and periodicity
115 are analysed by means of the Q-criterion and spectral analysis. The resulting data may contribute
116 to the assessment of reduced-order models and the unveiling of relevant flow mechanisms.

117 **NUMERICAL FRAMEWORK**

118 The in-house HYDRO3D LES code is used to solve the filtered Navier-stokes equations for an
119 unsteady, incompressible, viscous flow (Stoesser and Nikora 2008; Stoesser 2010; Bomminayuni
120 and Stoesser 2011; Stoesser et al. 2015; Fraga et al. 2016; Fraga and Stoesser 2016; Liu et al. 2016;
121 Ouro et al. 2017b). LES is an eddy-resolving technique in which the energetic portion of the flow
122 is simulated directly and only the sub-grid scale turbulence is modelled (Stoesser 2014), and is
123 therefore capable of explicitly predicting unsteadiness in flows of engineering importance (Koken
124 and Constantinescu 2009). The effects of the small-scale turbulence on the large eddies are cal-
125 culated using the Wall-Adapting Local Eddy-viscosity (WALE) sub-grid scale model introduced
126 by Nicoud and Ducros (1999). The diffusive terms are approximated by a fourth-order central
127 difference scheme while convective fluxes in the momentum and level-set equations are approxi-
128 mated using a fifth-order weighted, essentially non-oscillatory (WENO) scheme. A fractional-step
129 method is adopted with a Runge-Kutta predictor and the multigrid method is used to solve the
130 Poisson pressure-correction equation.

131 The Immersed Boundary Method (IBM), which maps Eulerian velocities onto Lagrangian

132 point-based representations of non-fluid bodies in the flow, is used to define the geometries of
 133 the abutments and bridge. The accuracy of the IBM for fluid-structure interaction is provided by:
 134 a) use of high-order convection-diffusion schemes; b) Eulerian-Lagrangian interpolation through
 135 delta-functions (Ouro and Stoesser 2017; Ouro et al. 2017a; Ouro et al. 2017b); c) high mesh reso-
 136 lution near solid boundaries. The position of the free surface is tracked using the Level Set Method
 137 developed by Osher and Sethian (1988), which defines a sharp air-water interface across which
 138 the density and viscosity transition smoothly through a level set signed distance function, ϕ , which
 139 has zero value at the phase interface and is negative in air and positive in water. This method is
 140 formulated as:

$$141 \quad \phi(x, t) < 0 \quad \text{if} \quad x \in \Omega_{gas} \quad (1)$$

$$143 \quad \phi(x, t) = 0 \quad \text{if} \quad x \in \Gamma \quad (2)$$

$$145 \quad \phi(x, t) > 0 \quad \text{if} \quad x \in \Omega_{liquid} \quad (3)$$

146 where Ω_{gas} and Ω_{liquid} represent the fluid domains for gas and liquid, respectively, and Γ is the
 147 interface. The LSM is proven successful in multiple two-phase flow studies (Sussman et al. 1994;
 148 Yue et al. 2006; Kang and Sotiropoulos 2012; McSherry et al. 2018).

149 **LABORATORY EXPERIMENTS AND NUMERICAL SETUP**

150 The computational setup shown in Fig. 1 replicates closely the physical experiments carried
 151 out at the Georgia Institute of Technology, US, similar to those presented in Hong et al. (2015).
 152 The physical model consists of a 24.4 m long steel flume of 4.26 m width and 0.76 m depth. It
 153 is an idealised hydraulic model of the Towaliga River bridge at Macon, Georgia which consists
 154 of flat horizontal floodplains on both sides of a main channel. Two spill-through abutments of
 155 depth 0.084 m, 2:1 slope and 0.636 m width with varying lengths are analysed in the large-eddy
 156 simulations. The shorter abutment (on the right floodplain) is the same length for both cases which
 157 extends to the edge of the main channel. At the left (downstream view) floodplain, two different
 158 abutment lengths, $0.41B_f$ and $0.77B_f$, are chosen - Long Setback (LSB) and Short Setback (SSB)
 159 cases respectively, where $B_f = 2.59m$ is the width of the left floodplain. The main channel is 0.96

160 m wide and extends streamwise along the whole length of the domain; it exhibits a parabolic cross-
161 section with a maximum depth of 0.13 m. The bridge deck (0.292 m wide and 0.033 m tall) sits on
162 top of the abutments and spans the full width of the channel. The numerical model duplicates the
163 geometries of the physical model except for a shorter streamwise length, which was compensated
164 by the use of a fully-developed flow inlet condition - explained in the paragraphs to follow. The
165 length of the computational domain is 15 m and 21 m in LSB and SSB respectively. These domain
166 lengths are chosen by running multiple attempts to make sure all large-scale recirculation and
167 turbulence downstream of the abutments are captured and are not affected by the outflow boundary
168 condition.

169 The conditions of the laboratory experiments are carefully replicated in the numerical simula-
170 tions. The discharge for LSB and SSB cases is set to $0.085m^3/s$ and $0.108m^3/s$ respectively. In the
171 experiment the water depth was controlled by a tailgate during the experiments to ensure a water
172 depth of 20 cm at the deepest part of the main channel under the bridge, and this condition was
173 ensured in the simulations. In such conditions, labelled as 'free flow scenario', the water surface
174 is not perturbed by the bridge at any point. The resulting bulk velocities are $U_b = 0.24m/s$ and
175 $0.29m/s$; the Reynolds numbers, based on the bulk velocity and four times the hydraulic radius
176 (Kara et al. 2012), are $Re = 76,300$ and $96,500$; finally, the global Froude numbers, based on U_b
177 and the average water depth D , are $Fr = 0.27$ and 0.32 for LSB and SSB cases respectively.

178 Fully developed turbulent inflow conditions are prescribed at the upstream boundary of the
179 domain. This is achieved by running precursor simulations in the absence of abutments and em-
180 ploying periodic boundaries. Once the flow achieves full development (based on first and second-
181 order statistics), the 3-D instantaneous flow field at one cross-section of the periodic channel is
182 recorded for 10,000 time steps and then provided as the inflow of the LSB and SSB simulations.
183 The precursor inflow velocity planes are recycled every 10,000 time steps, ensuring a continu-
184 ous fully-developed turbulent inflow for the duration of the simulation. This procedure has the
185 disadvantage of introducing periodicity in the turbulence field, which was judged not particularly
186 relevant due to the fact that the area of interest is located at or downstream of the contraction,

187 where the interaction with the abutments substantially alters the flow. Convective boundary condi-
188 tions are adopted at the outlet plane. No-slip boundary conditions are employed on the side walls
189 and channel bed while the level set method is applied to track the position of the free surface. The
190 initial free surface height, h is estimated based on the experimental measurements and is assumed
191 flat at the start of the simulation. The abutments, bridge, and the parabolic channel boundaries are
192 represented by a Lagrangian field of immersed boundaries.

193 Coarse and fine uniform numerical grids are generated for both scenarios. The coarse grid
194 (or mesh) for the LSB case comprises 1500x426x80 grid points in the streamwise, spanwise and
195 vertical directions, respectively, whereas the fine mesh doubles the resolution in all directions
196 resulting in 3000x852x160 grid points. The total number of grid points for the LSB cases are 51M
197 and 409M for coarse- and fine-mesh resolutions, respectively. The SSB case has the same mesh
198 resolution as the LSB in both coarse- and fine-mesh simulations but requires a longer domain in
199 the streamwise direction, resulting in 72M and 576M grid points, respectively. The number of
200 CPU cores required for the coarse- and fine-grid simulations are 300 and 1000, respectively for
201 both LSB and SSB cases. The coarse-grid simulations run for approx. 6 days while the fine-grid
202 simulations take approx. 12 days to achieve sufficiently averaged flow statistics.

203 **RESULTS AND DISCUSSION**

204 **Validation**

205 Profiles of computed and measured time-averaged streamwise velocity at the locations de-
206 scribed in Fig. 2 are plotted in Figs. 3 and 4 for LSB and SSB cases, respectively. The experimen-
207 tal velocities were measured with microADV probes; a detailed description of the ADV setup can
208 be found in Hong (2012). The validation points are located at five cross-sections: Up_toe(1) and
209 down_toe(4) at the upstream and downstream toes of the abutments respectively; Up_bridge(2)
210 and down_bridge(3) at the upstream and downstream faces of the bridge respectively; and
211 down_further(5), located 0.15 m downstream of down_toe. The intersections between the
212 aforementioned cross-sections (1)-(5) and the solid (for LSB) and dashed (for SSB) lines from
213 Fig. 2 provide the locations at which the time-averaged velocity profiles (a)-(h) exhibited in Figs.

214 3 and 4 are extracted. In Figs. 3 and 4, dashed horizontal lines show the approximate water surface
215 elevation at the corresponding location while solid horizontal lines represent the channel bed. The
216 vertical coordinate z is scaled with the initial water depth h at the deepest point ($h = 0.2039$ m for
217 LSB and $h = 0.2068$ m for SSB). Circles, dashed line and solid line represent the experimental, the
218 coarse-mesh LES and the fine-mesh LES data, respectively. For brevity only the validation profiles
219 at cross-sections 2, 3, and 4 are shown, the other two cross-sections are very similar in terms of the
220 match between experimental and numerical data. Also, for brevity only the streamwise velocity
221 validation is shown here, nevertheless LES-predicted spanwise and vertical velocity profiles were
222 also compared with experimental data and the overall agreement is found to be very similar to what
223 is reported in the following for the streamwise velocities.

224 The overall agreement between the experimental data and the LES results for the LSB case is
225 remarkably good. The predicted velocities match the measured ones quite well, except at the 3-4
226 (h) profiles, which are located in the vicinity of the right abutment, where the simulations overes-
227 timate the streamwise velocity by approximately 50%. This is probably due to slight differences
228 in the right abutment's geometry or slight location differences between experiments and simula-
229 tions. The numerical results obtained with the fine mesh (solid line) generally match better the
230 experimental measurements in all profiles except (a), where they tend to overestimate the veloci-
231 ties obtained in the laboratory. The fine-mesh LES performs very well in predicting the near-bed
232 streamwise velocity due to its higher resolution near the bed.

233 Fig. 4 allows quantitative comparisons of the simulated time-averaged streamwise velocity
234 profiles with the experimental data for the SSB case. The agreement between the coarse and fine
235 simulations is again convincing particularly in the main channel. Both grids seem to capture well
236 the details of the flow when subjected to a significant contraction. As with the LSB setup, the
237 velocities at some of the (h) profiles are overestimated by the LES in the vicinity of the right
238 abutment. There are no significant differences between the results for two mesh resolutions for
239 the most part, with the fine mesh slightly more accurate in the near-bed region, whereas the coarse
240 LES arguably shows somewhat better agreement at the upper half of some profiles at cross-sections

241 2 and 3. Profiles 3-4 (a) show significant discrepancies between both grid resolutions, probably
242 related to the fact that this location is under the influence of the shear layer produced by the left
243 abutment, and slight changes in its prediction have a great effect on the local velocities. It also
244 appears that the LES has achieved a reasonable grid convergence (the results of both meshes do
245 not offer significant differences). The succeeding plots in this paper are based on the data set
246 obtained from the fine-mesh simulations.

247 Figs. 5 and 6 present LES-computed water surface elevations together with experimental mea-
248 surement data at 15 locations along cross-sections 2, 3 and 4. The numerical data points are the
249 level set $\phi = 0$, which represents the relatively sharp boundary between the two fluids (water and
250 air). Overall, both LSB and SSB simulations provide a reasonable prediction of the water surface
251 elevation. The free surface is close to horizontal with a very gradual slope towards the right abut-
252 ment in the LSB case. The acceleration due to significant flow contraction of the SSB case results
253 in a water surface deformation, in the form of a depression near the abutments. The depression is
254 slightly more significant in the LES profile than in the experimental point gauge measurements.

255 **Flow Separation**

256 The instantaneous (a) and time-averaged (b) streamwise velocity contours for LSB and SSB
257 in a horizontal plane located 15 cm above the deepest point (2 cm above the floodplain bed) are
258 presented in Figs. 7 and 8. The dashed lines represent the zero streamwise velocity, hence high-
259 lighting the flow separation and recirculation downstream of the abutments. Several relevant flow
260 phenomena can be observed in these plots. Firstly, the effect of contraction: the flow acceler-
261 ates towards the abutments due to continuity, reaching at the contraction $2U_b$ in the LSB case and
262 $2.5U_b$ in the SSB case. Secondly, the abutment induces flow separation and a significant recircu-
263 lation bubble downstream of the abutments forms; the recirculation extends $x/b=1.82$ for LSB and
264 $x/b=2.39$ for SSB (see Fig. 9 for details) cases, respectively. Thirdly, the velocity contours reflect
265 rather clearly the banks of the main channel in the form of a velocity drop (white line), indicating
266 the impact of the secondary motion at the channel-floodplain interface on the streamwise veloc-
267 ity. Regarding the differences between the time-averaged and instantaneous streamwise velocity

268 fields, Figs. 7 and 8 rather nicely illustrate the distinctive scale of the medium-scale instantaneous
269 eddies versus the large-scale structures of the mean flow. The meandering motion induced by the
270 contraction on the flow in the main channel is particularly remarkable in the SSB case. Fig. 8a)
271 suggests that these oscillations at the main channel interface produce periodical ejections towards
272 the floodplains, particularly the left one.

273 2D (left) and 3D (right) streamlines are presented in Fig. 9 for LSB (top) and SSB (bottom)
274 cases. The two-dimensional flow field is extracted at a plane 15 cm above the deepest point of
275 the main channel; the 3D streamlines are colour-coded by the time-averaged streamwise velocity
276 $\langle u \rangle$. The flow separation is visualised and quantified and several recirculation zones occur. The
277 first one is located upstream of the abutments a result of the blockage they exert on the oncom-
278 ing flow. Small corner vortices are formed at the junction between the upstream toe and the side
279 walls, which are similar in size for both setups. The flow past the abutments is dominated by large
280 recirculation cells featuring counter-clockwise rotating vortices in both cases. The left abutment's
281 recirculation of the SSB case extends much further downstream and reaches $x/b = 2.39$ before
282 the flow reattaches to the side wall, whereas for LSB (shorter left abutment) the flow reattaches
283 at approx. $x/b = 1.82$. Comparing both cases, the ratio between the lengths of the recircula-
284 tion bubbles $\frac{X_{SSB}}{X_{LSB}} = 1.3$ is significantly smaller than the ratio between the left abutments' lengths
285 $\frac{0.77B_f}{0.41B_f} = 1.9$, but rather similar to the ratio between the maximum velocities $\frac{U_{SSB}}{U_{LSB}} = 1.25$. These
286 counter-clockwise eddies are complemented by corner vortices (labeled CV1 and CV2) at the
287 downstream junction of the left abutment which rotate in the clockwise direction. Interestingly,
288 while CV1 covers the whole length of the abutment, CV2 is more constrained towards the side
289 wall, which may be explained by the dominance of the main recirculation cell. The larger con-
290 traction ratio of the SSB case causes the flow to veer more substantially towards the right side of
291 the main channel; the streamlines are diverted almost immediately after the bridge opening onto
292 the right floodplain and flow reattachment takes place at $x/b = 0.765$. For the LSB case, the main
293 channel is not deflected towards the right bank and hence the reattachment does not occur until
294 $x/b = 0.884$, allowing a slightly larger and more defined recirculation eddy behind the right abut-

295 ment in comparison with the rather short compressed recirculation zone of the LSB case. Figs.
 296 9c and 9d highlight again the difference in extent of recirculation between cases and also visu-
 297 alise the significant flow acceleration that takes place through the opening and high velocities are
 298 sustained until the end of the respective recirculation zones. The similarities of the vortical struc-
 299 tures' shapes and sizes between the 2D and 3D figures demonstrate that the flow is predominantly
 300 two-dimensional in the shallow floodplains.

301 **Instantaneous Secondary Flow**

302 The previous section discussed the main features of the time-averaged flow separation and
 303 recirculation bubbles behind the abutments. However, in the context of a turbulent flow, the shape
 304 and size of these coherent structures is subjected to the interaction with transitory structures which
 305 provoke oscillations and meandering (see Fig. 8a), resulting in increased turbulence. Of particular
 306 interest is the region behind the abutments which is where three turbulence structures interact: a)
 307 the shear layer between the recirculation zones and the main flow, b) the vortices shed from the
 308 abutments' tip, c) the transition between the main channel and the floodplain.

309 Fig. 10 presents isosurfaces of the Q-criterion together with vorticity contours in selected
 310 cross-sections. The Q-criterion (e.g. (Dubief and Delcayre 2000)) is defined as:

$$311 \quad Q = \frac{1}{2}(|\Omega| - |S|) \quad (4)$$

312 in which $|\Omega|$ and $|S|$ are the rotation and strain rates, respectively:

$$313 \quad |\Omega| = \sum_{i,j=1}^3 \left[\frac{1}{2} \left(\frac{\partial u_i}{\partial x_j} - \frac{\partial u_j}{\partial x_i} \right) \right]^2 \quad (5)$$

$$314 \quad |S| = \sum_{i,j=1}^3 \left[\frac{1}{2} \left(\frac{\partial u_i}{\partial x_j} + \frac{\partial u_j}{\partial x_i} \right) \right]^2 \quad (6)$$

316 where u_i and u_j are instantaneous velocity components. Positive isosurfaces of Q isolate areas
 317 where the strength of rotation overcomes the strain, thus visualising rotation in the form of vortex
 318 tubes. The Q-criterion isosurfaces are colour-coded with the streamwise vorticity ω_x , which mea-

319 sures the rotation intensity around the streamwise x axis, hence on the YZ cross-sectional plane.
320 Positive streamwise vorticity (red) corresponds to clockwise rotation while blue represents anti-
321 clockwise motion. The Q -criterion isosurfaces are complemented with three cross-sectional slices
322 of the ω_x field in between and downstream of the abutments to help understand the secondary
323 motion. The vortex tubes labelled SSL are shed from the tip of the abutments and then convected
324 downstream along the shear layer formed between the accelerated flow through the opening and
325 the recirculating, low-momentum zones of the floodplains and downstream of the abutments. The
326 NV label identifies 'necklace vortices', which can be found near the abutments as an offset of the
327 SSLs towards the main channel. NVs form before approaching the abutments, more noticeably for
328 the right abutment in both cases. NVs are better defined and exhibit a more consistent streamwise
329 vorticity colouring than SSLs, i.e. they portray their stable rotating motion (clockwise by the left
330 abutment and anti-clockwise by the right one). In both LSB and SSB cases, a long patch of inter-
331 face vortices (IV) appear as a result of the momentum exchange between the right edge of the main
332 channel and the floodplain; starting upstream of the right abutment as the flow is forced into the
333 main channel. The same flow mechanism produces a very well-defined IV at the interface between
334 the main channel and the left floodplain but only for the SSB case (Fig. 10b). In the LSB case (Fig.
335 10a), no IV is found on the left side of the main channel, highlighting the differences between the
336 two contraction ratios. Interestingly, a counter-rotating vortex pair near the water surface labelled
337 as SV can only be found in the LSB results. The SV pair consists of both short clockwise and
338 long anti-clockwise rotating vortices side by side near the surface and off centre towards the left of
339 the main channel. When visualising simultaneously instantaneous velocity streamlines (not shown
340 for clarity and brevity), the SV pair forms where the surface flow coming from the left and right
341 floodplains meet over the main channel.

342 Fig. 11 presents three-dimensional views of the water surface ($\phi = 0$ level-set isosurface) at an
343 instant in time for the LSB and SSB cases, respectively. The vertical axis is exaggerated by a factor
344 of 10 to highlight better the features of the water surface deformations. The coherent structures
345 described in Fig. 10 have a clear signature at the free surface; regularly recurring dips in the water

346 surface are the low-pressure core of the shear layer vortices in both cases, although the dips are
347 more prominent in the SSB geometry due to a stronger shear layer and vortices. The effect of the
348 SV on the free surface of the LSB setup is very noticeable and it appears in Fig. 11a) as a persistent
349 bulging line.

350 **Shear Layer Oscillation and Vortex Shedding**

351 With the aim of quantifying the oscillations and the vorticity generated in the shear layer be-
352 hind the abutments for different contraction ratios, several timeseries' of velocity are recorded at
353 selected sampling points for both LSB and SSB cases over a relatively long period of simulation
354 time (approx. 150 seconds which corresponds to 2-3 flow through times) and at a frequency of
355 500Hz. The time-series obtained are analysed using: probability density function, quadrant anal-
356 ysis and power density spectra, and the data are related to the physics of the instantaneous flow.
357 The probability density function is calculated by first, sorting the recorded signal of streamwise
358 velocity fluctuations, u' into bins of uniform intervals to obtain a histogram of the data signal. The
359 area of each histogram bin is then divided by the total area of the histogram, giving the probability
360 density function of the time series.

361 Fig. 12a depicts the locations where velocity time signals are recorded for the LSB case with
362 L and R being the label for those points in the vicinity of the left or right abutment, respectively.
363 The probability density function (PDF) of the turbulent fluctuation of the streamwise velocity u' ,
364 normalised by its root-mean-square value u'_{RMS} is calculated at each sampling point and plotted
365 together with the Gaussian distribution (solid line). Fig. 12b plots the pdfs for the LSB's left abut-
366 ment and as can be seen almost all the pdfs exhibit a skewness towards the positive except for the
367 pdf at L1 which follows the Gaussian distribution fairly well. L1 is located in the vicinity of the tip
368 of the abutment, where the separation begins. From L2 onwards, the pdfs show a clear deviation of
369 the mean u'/u'_{RMS} from Gaussian towards the positive side, centred around $u'/u'_{RMS} = 0.4$ approx.
370 The amplitude of the u' fluctuations is also skewed, ranging from $u'/u'_{RMS} = -4$ on the negative
371 side of the axis to less than $u'/u'_{RMS} = 3$ on the positive values. This suggests that the flow at these
372 locations feature many acceleration slightly stronger (than the average) accelerations due to the

373 bridge contraction (hence the positive u'/u'_{RMS} mean from L2 onwards) combined with more sig-
374 nificant low frequency events in which the recirculation bubble expands into the shear layer along
375 which points L2-L8 are located (hence the long negative tail of the PDFs). The seven R points
376 located in the shear layer of the right abutment (Fig. 12c) follow quite closely the normal distri-
377 bution, although with a very slight bias towards the negative side and a very slight tailing towards
378 the positive side. This indicates a lower occurrence of high-momentum ejections from the right
379 abutment's tip and a more balanced equilibrium between the recirculation and the main channel
380 flow overall. The different turbulence characteristics in terms of streamwise velocity fluctuation of
381 the flow around the two abutments is the consequence of the different abutment length (however
382 not very significant in the LSB case) and the geometrical asymmetry of the compound channel; the
383 left floodplain is much wider and carries more mass and momentum so that flow acceleration due
384 to contraction is more significant in the shear layer of the left abutment than in the one of the right
385 abutment.

386 Fig. 13 shows the locations where velocity time signals are recorded and the corresponding
387 u'/u'_{RMS} pdfs for the SSB case. Overall, the pdfs at those points follow but amplify the trends
388 from the LSB case, as it is expected given the greater contraction ratio. From the u'/u'_{RMS} pdfs
389 along the left shear layer (L locations), only L2 appears to be Gaussian distributed. All other L
390 signals exhibit a clear skewness, following the normal distribution up to $u'/u'_{RMS} = -1$, having a
391 maximum at approx. $u'/u'_{RMS} = 0.75$ and then falling abruptly. The exception is L3, which peaks at
392 approximately $u'/u'_{RMS} = -0.6$. L3 is situated at the point where small vortical eddies start to form
393 shortly after the flow separates from the abutment tip. The behaviour of the points L2 and L4-L9
394 correlates with the frequent occurrence of ejections of high momentum flow (local accelerations)
395 from the opening and low frequency events occur due to the expansion of the recirculation zone
396 similar the LSB case. The meandering of the instantaneous velocities in the SSB setup as observed
397 in Fig. 8a is the direct result of the oscillating recirculation zone. The pdfs at the locations near the
398 right abutment (Fig. 13c) mostly follow the Gaussian distribution, except for R4 and R5 which are
399 rather biased towards negative values on the u'/u'_{RMS} axis. This suggests a stronger recirculation

400 behind the right abutment that pushes the shear layer towards the main channel when compared to
401 the LSB results. This correlates well with the observations made from Fig. 9b.

402 The quadrant analysis of the streamwise u'/u'_{RMS} and spanwise v'/v'_{RMS} velocity fluctuations
403 are plotted in Figs. 14 and 15 for the LSB or SSB cases, respectively. Unlike the conventional
404 quadrant analysis (Lu and Willmarth 1973) that investigates the sweeping and ejecting motion of
405 the flow near the bed, here the analysis focuses on the horizontal turbulence events of the stream-
406 wise and spanwise directions in the separated shear layers. For brevity, only four points from
407 each abutment are chosen and to be displayed and the vertical fluctuations w'/w'_{RMS} were omitted
408 given the strong two-dimensional nature of the recirculations and the shear layers on the shallow
409 floodplains. The location of the points is indicated in Figs. 12a and 13a, assuming positive direc-
410 tions for u'/u'_{RMS} and v'/v'_{RMS} east (flow towards the outlet) and north (flow towards the left side),
411 respectively.

412 Fig. 14 shows the quadrant analysis for the LSB case. Points L3, L5, and L7 confirm the
413 findings from Fig. 12b, with most points concentrated in Q1 ($u'/u'_{RMS} > 0, v'/v'_{RMS} > 0$) corre-
414 sponding to fast-flow ejections from the contracted flow through the bridge opening, and fewer but
415 higher-magnitude points recorded in Q3 ($u'/u'_{RMS} < 0, v'/v'_{RMS} < 0$), indicating lower-frequency
416 intrusions of the recirculating flow in the shear layer. L1 exhibits a more balanced, isotropic trend,
417 characterised by an oval shape which is characteristic of streamwise fluctuations. Points R3, R5,
418 and R7 reproduce a more balanced oval shape dominated by Q2 and Q4 events ($u'/u'_{RMS} < 0$ -
419 $v'/v'_{RMS} > 0$ and $u'/u'_{RMS} > 0$ - $v'/v'_{RMS} < 0$ respectively), as the relative position of floodplain and
420 main channel switches from left to right abutment. Point R1, by the flow around abutment's tip has
421 a slight tendency for Q2 and Q4 events but it is more isotropic than the other locations.

422 Fig. 15 shows the quadrant analysis for the SSB case. The data sampled at the L locations (left
423 abutment) show three different patterns. At location L1, by the abutment tip, the data points show
424 significant linearity in the axis Q2-Q4 ($u'/u'_{RMS} < 0$ - $v'/v'_{RMS} > 0$ and $u'/u'_{RMS} > 0$ - $v'/v'_{RMS} < 0$,
425 respectively), revealing an almost one-dimensional flow, resembling a jet, as the water from the
426 left floodplain is forced to pass around the abutment. At location L3 at which eddys start to form,

427 a more balanced, isotropic behaviour of the flow is observed, with a slight majority of turbulent
 428 events in Q3 ($u'/u'_{RMS} < 0, v'/u'_{RMS} < 0$) and fewer and more dispersed points in Q1 ($u'/u'_{RMS} > 0,$
 429 $v'/u'_{RMS} > 0$), indicating a dominance of the recirculation bubble at this location, with periodic
 430 intrusions of high-speed flow from the contraction, in agreement with the observations from Fig.
 431 13b. The data at locations L5 and L7 are similarly in their oval shape and clustered around the
 432 u'/u'_{RMS} axis. The higher flow contraction induces strong acceleration and hence significant one-
 433 dimensionality of the flow, albeit the shift between positive and negative values of u'/u'_{RMS} reflects
 434 the meandering of the shear layer in the left abutment's shear layer. The flow is significantly
 435 anisotropic with u' having a greater variance than v' . Near the right abutment, the flow at R1
 436 appears similar the flow at L1 (switching the axis from Q2-Q4 to Q1-Q3 due to the opposite
 437 orientation of the abutment) but is not quite as one-dimensional than at L1. At R3 the data show a
 438 rather isotropic distribution of turbulent events, that turns into an oval shape in the axis Q2-Q4 for
 439 R5 and R7 as small eddies roll up and being less one-dimensional than their left side counterparts.

440 Figs. 16-18 and Fig. 20 offer further insights into the turbulence structure at two chosen
 441 locations (L7 and R5) near each abutment and for both cases. Each figure consists of four sub-
 442 plots, from top-left to bottom-right: (a) power spectra of both the streamwise u' and the spanwise v'
 443 turbulent fluctuations in the domain of frequency (logarithmic scale) obtained through Fast Fourier
 444 Transformation; (b) power spectra in a semilog plot to identify high-energy events; (c) out-of-plane
 445 vorticity contours ω_z , with white contours representing strong anti-clockwise motion ($\omega_z < 0$)
 446 and black contours representing strong clockwise motion ($\omega_z > 0$) (contours extracted at 0.015 m
 447 below the water surface); (d) top view of the water surface ($\phi = 0$) at the same instant as in (c) to
 448 illustrate the correlation between the out-of-plane vorticity and the free surface undulation. The
 449 free surface is colour-coded with water depth where dark blue depicts the depressions in the water
 450 surface.

451 The power spectra from all four points (Figs. 16a - 18a and 20a) follow the $-5/3$ slope, indi-
 452 cating homogenous turbulence, before a faster decay of energy is observed at higher frequencies
 453 which is mainly induced by the SGS model. The plots demonstrate that the inertial sub-range

454 of the energy cascade for u' and v' is well resolved that the fine mesh resolves satisfactorily the
455 energy-containing scales of the flow. In total over two frequency decades of the flow, between the
456 production of energetic large-scale vortices and the dissipation of the small scale turbulence are
457 resolved by the LES of both cases.

458 Fig. 16 reveals the vortex shedding at L7, located downstream of the left abutment of the
459 LSB setup. The power spectra of u' and v' at L7 show a very distinct peak at approximately 0.1
460 Hz, revealing the persistent occurrence of a turbulent event with a 10 s periodicity. This peak is
461 particularly well depicted in Fig. 16b, where the logarithmic scale for the spectral amplitude of the
462 velocity signal has been removed. This event captured in the spectral analysis is a vortex that rolls
463 up in the shear layer downstream of the left abutment which is convected downstream. The area of
464 high vorticity ω_z in Fig. 16c and the depressions in the water surface map Fig. 16d (indicated with
465 arrows) visualise two of these vortices each at a different stage their evolution. The vortex closer
466 to the abutment (above the left arrow) has just rolled up whereas the vortex further downstream
467 (above right arrow) has reached its maximum size and is being convected by the flow downstream.
468 The average period of occurrence of this vortex is approximately 10 s. The vortex can also be
469 identified from the quadrant analysis at L7 (Fig.14), where the dominant high-frequency $u' > 0$
470 ejections are complemented with few but significant (low-frequency) $u' < 0$ events the signature
471 of the passing vortex.

472 Fig. 17 quantifies periodical turbulent events at R5, i.e. downstream of the right abutment of
473 the LSB case. The u' spectrum (Figs. 17a-b) exhibits two high-energy peaks which correspond to
474 approx. 10s and 6.2s periodicity (or in terms of frequency to 0.1 Hz and 0.16 Hz, respectively).
475 The latter peak is also seen in the v' spectrum. The ω_z contours and water surface maps (Figs.
476 17c-d) reveal vortex roll-up and shedding from the tip of the abutment, albeit more irregular than
477 around the left abutment. The vortex generation and roll-up are highlighted with arrows in Figs.
478 17c-d. Unlike the left abutment, there appears to be a bi-modality in the vortex formation, also just
479 noticeable in the equivalent pdf (12c). This bi-modal behavior is probably due the interaction of the
480 vortex with the secondary flow near the main channel-floodplain interface, dominated by the SSL,

481 IV and NV vortices described in Fig. 10.

482 Fig. 18 reveals large-scale turbulence at L7, downstream of the left abutment of the SSB case.
483 The u' energy spectra (Figs. 18a-b) exhibit a very prominent low-frequency peak at 0.1 Hz (10
484 s period). However, the vortices (Figs. 18c) do not appear to roll-up into distinct eddies such as
485 those seen behind the LSB abutment, but rather are stretched due to the strong acceleration and
486 stay within a narrow band along the shear layer. The water surface elevation plot (Fig. 18d) does
487 not depict significant depressions suggesting the absence of a well-defined eddy downstream of
488 the left abutment and this can also be concluded from the fact that the v' spectra do not show any
489 low-frequency peak. Moreover, the quadrant analysis (Fig. 15) also reveals the jet-like accelera-
490 tion (almost one-dimensional flow) due to the narrow bridge opening with significantly greater u'
491 than v' values. From animations of the flow downstream of the abutment it is seen that the 10s-
492 periodicity correlates with a low-frequency meandering of the main channel flow as visualised by
493 the instantaneous streamwise velocity flow field depicted in Fig. 8a.

494 Fig. 19 (top) shows a time series of the instantaneous streamwise velocity at L7 where distinc-
495 tive high- and low-velocity peaks occur approximately every 10 s. The instantaneous streamwise
496 velocity u contours at the six instants in time labelled in the time series (t_1 - t_6) are also presented
497 below the timeseries to illustrate the shift between high velocities (dominant most of the time)
498 and sudden low velocity peaks (at t_2 , t_4 and t_6). Two black lines representing 0.2 m/s and 0.4 m/s
499 contours are included in the figure to highlight the boundary between the recirculation bubble and
500 the main flow. This boundary oscillates due to the combination of the vorticity generated by the
501 ejections from the bridge opening and the secondary flow at the main channel-floodplain interface,
502 resulting in the characteristic 0.1 Hz meandering motion.

503 The turbulence characteristic at R5, downstream of the right abutment of the SSB case, is
504 revealed with Fig. 20. The power spectra (Figs. 20a-b) show multiple peaks ranging from 0.1
505 Hz to 0.47 Hz, that can be correlated with several eddies (with periods between 2-10 s approx.)
506 springing off the right abutment's tip as can be appreciated from Figs. 20c-d. The flow in this
507 location is similar to the one behind the LSB abutment, however the relatively small peaks in the

508 v' spectra indicate that the flow accelerates at the right abutment in a similar fashion to the left
509 abutment, which leads to more irregular shedding of vortices. The irregularity of vortex shedding
510 is, similarly to the LSB case, due to the interplay of SSL, IV and NV vortices.

511 **CONCLUSION**

512 In this study the method of large eddy simulation (LES) has been employed to elucidate and
513 quantify the flow and associated turbulence structures around bridge abutments of different lengths,
514 i.e. a long setback (LSB) abutment and a short setback (SSB) abutment, which are placed in a com-
515 pound and asymmetric channel. A free surface algorithm has been included in the LES which has
516 allowed predicting the free-surface deformation of the two investigated scenarios. Experimental
517 data has been used to validate the two simulations and very convincing agreement of computed
518 streamwise velocity profiles with the measured ones has been found. Similarly good agreement
519 of LES-computed water surface elevations with experimental data has been observed and has thus
520 established the credibility of the numerical method. The simulations have allowed the quantifica-
521 tion of the effect of the abutment length on the flow and turbulence through and behind the bridge
522 opening. Moreover, instantaneous and time-averaged streamwise velocity contours have been plot-
523 ted and analysed to reveal several key differences between the SSB and LSB flow scenarios: a) a
524 significantly larger recirculation zone downstream of the left abutment but a smaller corner vortex
525 in in SSB scenario in comparison with the LSB scenario; b) the main channel flow in the SSB
526 scenario is skewed more clearly towards the right bank due to the more accelerated flow and the
527 larger recirculation zone downstream of the abutment of the SSB scenario; and c) more significant
528 meandering of the flow downstream of the abutment in the SSB scenario. In addition, turbulence
529 structures, such as rolled-up shear layer-, necklace- and interface vortices due to the secondary
530 flow, generated by the abutments and/or the compound channel geometry, respectively, have been
531 visualised using isosurfaces of the Q-criterion and out-of-plane vorticity contours. The differences
532 between the LSB and SSB flow scenarios are: a) only in the SSB scenario, a very well-defined
533 longitudinal (or streamwise) vortex is found at the interface between the main channel and the left
534 floodplain; b) only in the LSB scenario, a pair of counter-rotating vortices appears near the surface

535 in the vicinity of the left floodplain, being reflected in the free surface deformation in the form of
536 a persistent bulging line. Further analysis of the prevailing turbulence structures has been carried
537 out using three different techniques: probability density functions, quadrant analysis and power
538 density spectra. The analyses of the time series of instantaneous velocity signals has quantified the
539 complex turbulent flow near the abutments including: a) frequent occurrence of ejections of high
540 momentum flow in the form of vortices springing-off of the tip of the abutment and rolling-up into
541 low-frequency horizontal vortices in the vicinity of the long setback abutment and b) domination
542 of strongly-accelerated flow in the vicinity of the short setback abutment due to the higher con-
543 traction. This jet-like flow is pretty-much one-dimensional and persists over a substantial distance
544 downstream. c) wake-meandering flow downstream of the short-setback abutment and d) irregu-
545 lar vortex generation and shedding at the right abutment (in both cases) due to the interaction of
546 main-channel/floodplain interface vortices.

547 **ACKNOWLEDGEMENT**

548 This work was sponsored by the American Association of State Highway and Transportation
549 Officials (AASHTO), in cooperation with the Federal Highway Administration, and was conducted
550 in the National Cooperative Highway Research Program (NCHRP), which is administered by the
551 Transportation Research Board (TRB) of the National Academics of Sciences, Engineering, and
552 Medicine. The authors acknowledge the support of the Supercomputing Wales project, which is
553 part-funded by the European Regional Development Fund (ERDF) via Welsh Government

NOTATION

The following symbols are used in this paper:

Fr = Froude number;

ϕ = level set signed distance function;

Ω_{gas} = Fluid domain for gas;

Ω_{liquid} = Fluid domain for water;

Γ = Water surface interface;

B_f = Left floodplain width;

U_b = Bulk streamwise velocity;

Re = Reynolds number;

h = Initial free surface height;

b = Width of channel;

x/b = Streamwise distance normalised by width of channel;

u = Instantaneous streamwise velocity;

$\langle u \rangle$ = Time-averaged streamwise velocity;

X_{LSB} = Time-averaged length of recirculation bubbles in LSB;

X_{SSB} = Time-averaged length of recirculation bubbles in SSB;

U_{LSB} = Maximum streamwise velocity in LSB;

U_{SSB} = Maximum streamwise velocity in SSB;

Q = Q-criterion;

$|\Omega|$ = Rotation rate;

$|S|$ = Strain rate;

u_i, u_j = Instantaneous velocity components;

ω_x = Streamwise vorticity;

u' = Turbulent fluctuation of streamwise velocity;

u'_{RMS} = Root-mean-square of turbulent fluctuation of streamwise velocity; and

v' = Turbulent fluctuation of spanwise velocity.

REFERENCES

- Bomminayuni, S. K. and Stoesser, T. (2011). "Turbulence Statistics in an Open-Channel Flow over a Rough Bed." *Journal of Hydraulic Engineering*, 137(11), 1347–1358.
- Cater, J. E. and Williams, J. J. R. (2008). "Large eddy simulation of a long asymmetric compound open channel." *Journal of Hydraulic Research*, 46(4), 445–453.
- Dubief, Y. and Delcayre, F. (2000). "On coherent-vortex identification in turbulence." *Journal of Turbulence*, 1(January), 1–22.
- Ettema, R., Nakato, T., and Muste, M. (2010). "Estimation of Scour Depth At Bridge Abutments." *Report No. January*, The University of Iowa, Iowa.
- Fael, C. M. S., Simarro-Grande, G., Martín-Vide, J. P., and Cardoso, A. H. (2006). "Local scour at vertical-wall abutments under clear-water flow conditions." *Water Resources Research*, 42(10), 1–12.
- Fraga, B. and Stoesser, T. (2016). "Influence of bubble size, diffuser width, and flow rate on the integral behavior of bubble plumes." 121, 3887–3904.
- Fraga, B., Stoesser, T., Lai, C. C. K., and Socolofsky, S. A. (2016). "A LES-based Eulerian-Lagrangian approach to predict the dynamics of bubble plumes." *Ocean Modelling*, 97, 27–36.
- Hong, S. H. (2012). "Prediction of Clear-Water Abutment Scour Depth in Compound Channel for Extreme Hydrologic Events." Ph.D. thesis, Georgia Institute of Technology, <<https://smartech.gatech.edu/handle/1853/47535>> (dec).
- Hong, S. H., Sturm, T. W., and Stoesser, T. (2015). "Clear Water Abutment Scour in a Compound Channel for Extreme Hydrologic Events." *Journal of Hydraulic Engineering*, 141(6).
- Kang, S. and Sotiropoulos, F. (2012). "Numerical modeling of 3D turbulent free surface flow in natural waterways." *Advances in Water Resources*, 40, 23–36.
- Kara, S., Kara, M. C., Stoesser, T., and Sturm, T. W. (2015). "Free-Surface versus Rigid-Lid LES Computations for Bridge-Abutment Flow." *Journal of Hydraulic Engineering*, 141(9).
- Kara, S., Stoesser, T., and Sturm, T. W. (2012). "Turbulence statistics in compound channels with deep and shallow overbank flows." *Journal of Hydraulic Research*, 50(5), 482–493.

584 Koken, M. (2011). “Coherent structures around isolated spur dikes at various approach flow an-
585 gles.” *Journal of Hydraulic Research*, 49(6), 736–743.

586 Koken, M. (2017). “Coherent structures at different contraction ratios caused by two spill-through
587 abutments.” *Journal of Hydraulic Research*, homepage, 22–1686.

588 Koken, M. and Constantinescu, G. (2008a). “An investigation of the flow and scour mechanisms
589 around isolated spur dikes in a shallow open channel: 1. Conditions corresponding to the initia-
590 tion of the erosion and deposition process.” *Water Resources Research*, 44(8), 1–19.

591 Koken, M. and Constantinescu, G. (2008b). “An investigation of the flow and scour mechanisms
592 around isolated spur dikes in a shallow open channel: 2. Conditions corresponding to the final
593 stages of the erosion and deposition process.” *Water Resources Research*, 44(8).

594 Koken, M. and Constantinescu, G. (2009). “An investigation of the dynamics of coherent structures
595 in a turbulent channel flow with a vertical sidewall obstruction.” *Physics of Fluids*, 21(8).

596 Koken, M. and Constantinescu, G. (2014). “Flow and Turbulence Structure around Abutments with
597 Sloped Sidewalls.” *Journal of Hydraulic Engineering*, 140(7), 04014031.

598 Laursen, E. M. (1963). “An analysis of relief bridge scour.” *Journal of the Hydraulics Division*.

599 Lin, C., Han, J., Bennett, C., and Parsons, R. L. (2014). “Case History Analysis of Bridge Failures
600 due to Scour.” *Climatic Effects on Pavement . . .*, 1–13.

601 Liu, Y., Stoesser, T., Fang, H., Papanicolaou, A., and Tsakiris, A. G. (2016). “Turbulent flow over
602 an array of boulders placed on a rough, permeable bed.” *Computers and Fluids*, 158, 120–132.

603 Lu, S. S. and Willmarth, W. W. (1973). “Measurements of the structure of the Reynolds stress in a
604 turbulent boundary layer.” *Journal of Fluid Mechanics*, 60(03), 481.

605 McSherry, R., Chua, K., Stoesser, T., and Mulahasan, S. (2018). “Free surface flow over square
606 bars at intermediate relative submergence.” *Journal of Hydraulic Research*, 1–19.

607 Melville, B. W. (1992). “Local scour at bridge piers.” *Journal of Hydraulic Engineering*, 118(4),
608 615–631.

609 Melville, B. W. (1995). “Bridge Abutment Scour in Compound Channels.” *Journal of Hydraulic
610 Engineering*, 121(12), 863–868.

611 Nicoud, F. and Ducros, F. (1999). “Subgrid-scale stress modelling based on the square of the
612 velocity gradient tensor.” *Flow, turbulence and Combustion*, 62(3), 183–200.

613 Osher, S. and Sethian, J. A. (1988). “Fronts propagating with curvature-dependent speed: Al-
614 gorithms based on Hamilton-Jacobi formulations.” *Journal of Computational Physics*, 79(1),
615 12–49.

616 Ouro, P., Harrold, M., Stoesser, T., and Bromley, P. (2017a). “Hydrodynamic loadings on a hori-
617 zontal axis tidal turbine prototype.” *Journal of Fluids and Structures*, 71, 78–95.

618 Ouro, P. and Stoesser, T. (2017). “An immersed boundary-based large-eddy simulation approach
619 to predict the performance of vertical axis tidal turbines.” *Computers & Fluids*, 152, 74–87.

620 Ouro, P., Wilson, C. A., Evans, P., and Angeloudis, A. (2017b). “Large-eddy simulation of shallow
621 turbulent wakes behind a conical island.” *Physics of Fluids*, 29(12).

622 Paik, J. and Sotiropoulos, F. (2005). “Coherent structure dynamics upstream of a long rectangular
623 block at the side of a large aspect ratio channel.” *Physics of Fluids*, 17(11), 1–14.

624 Rodi, W., Constantinescu, G., and Stoesser, T. (2013). *Large-eddy simulation in hydraulics*. Crc
625 Press.

626 Shirole, A. and Holt, R. (1991). “Planning for a comprehensive bridge safety assurance program.”
627 *Transport Research Record*, Vol. 1290, 137–142.

628 Stoesser, T. (2010). “Physically Realistic Roughness Closure Scheme to Simulate Turbulent Chan-
629 nel Flow over Rough Beds within the Framework of LES.” *Journal of Hydraulic Engineering*,
630 136(10), 812–819.

631 Stoesser, T. (2014). “Large-eddy simulation in hydraulics: Quo Vadis?.” *Journal of Hydraulic
632 Research*, 52(4), 441–452.

633 Stoesser, T., McSherry, R., and Fraga, B. (2015). “Secondary Currents and Turbulence over a
634 Non-Uniformly Roughened Open-Channel Bed.” *Water*, 7(9), 4896–4913.

635 Stoesser, T. and Nikora, V. (2008). “Flow structure over square bars at intermediate submergence:
636 Large Eddy Simulation study of bar spacing effect.” *Acta Geophysica*, 56(3), 876–893.

637 Sturm, T. W. (2006). “Scour around Bankline and Setback Abutments in Compound Channels.”

638 *Journal of Hydraulic Engineering*, 132(1), 21–32.

639 Sturm, T. W. and Janjua, N. S. (1994). “Clear-water Scour Around Abutments in Floodplains.”

640 *Journal of Hydraulic Engineering*, 120(8), 956–972.

641 Sumer, B. M. and Fredsøe, J. (2002). *The Mechanics of Scour in the Marine Envi-*

642 *ronment*, Vol. 17 of *Advanced Series on Ocean Engineering*. WORLD SCIENTIFIC,

643 <<http://www.worldscientific.com/worldscibooks/10.1142/4942>> (apr).

644 Sussman, M., Smereka, P., and Osher, S. (1994). “A Level Set Ap-

645 proach for Computing Solutions to Incompressible Two-Phase Flow,

646 <<http://www.sciencedirect.com/science/article/pii/S0021999184711557>>.

647 Wardhana, K. and Hadipriono, F. C. (2003). “Analysis of Recent Bridge Failures in the United

648 States.” *Journal of Performance of Constructed Facilities*, 17(3), 144–150.

649 Xie, Z., Lin, B., and Falconer, R. A. (2013). “Large-eddy simulation of the turbulent structure in

650 compound open-channel flows.” *Advances in Water Resources*, 53, 66–75.

651 Yue, W., Lin, C.-L., and Patel, V. C. (2005). “Large eddy simulation of turbulent open-channel

652 flow with free surface simulated by level set method.” *Physics of Fluids*, 17(2), 025108.

653 Yue, W., Lin, C.-L., and Patel, V. C. (2006). “Large-Eddy Simulation of Turbulent Flow over a

654 Fixed Two-Dimensional Dune.” *Journal of Hydraulic Engineering*, 132(7), 643–651.

655
656
657
658
659
660
661
662
663
664
665
666
667
668
669
670
671
672
673
674
675
676
677
678
679
680

List of Figures

1	Computational domains: (a) Long-setback abutment case, LSB, (b) Short-setback abutment case, SSB, (c) Cross-section including its dimensions.	30
2	Definition sketch of the abutments and bridge area. The intersections between horizontal numbered lines (1-5) and vertical solid (LSB) and dashed (SSB) lines indicate the locations at which time-averaged streamwise velocity profiles (a)-(h) were measured experimentally.	31
3	Computed and measured time-averaged streamwise velocity profiles at locations (a)-(h) (as described in Fig. 2) in cross-sections 2-4 of the LSB case. Experimental data (circles), coarse-mesh LES (dashed line), and fine-mesh LES (solid line). . . .	32
4	Computed and measured time-averaged streamwise velocity profiles at locations [a]-[h] (as described in Fig. 2) in cross-sections 2-4 of the SSB case. Experimental data (circles), coarse-mesh LES (dashed line), and fine-mesh LES (solid line). . . .	33
5	Computed (solid line) and measured (circles) profiles of the water surface for the LSB case at cross-section 2-4.	34
6	Computed (solid line) and measured (circles) profiles of the water surface for the SSB case at cross-section 2-4.	35
7	LES-predicted streamwise velocity contours in a selected horizontal plane: (a) instantaneous (b) time-averaged velocity for the LSB case.	36
8	LES-predicted streamwise velocity contours in a selected horizontal plane: (a) instantaneous (b) time-averaged velocity for the SSB case.	37
9	2D streamlines near the abutment for (a) the LSB case and (b) the SSB case, 3D streamlines colour-coded with time-averaged streamwise velocity for (a) the LSB case and (b) the SSB case.	38
10	Isosurfaces of the Q-criterion together with contours of the streamwise vorticity in selected cross-sections: (a) LSB case, (b) SSB case.	39

681	11	Water surface deformation represented by zero level set and colour-coded by water	
682		depth for (a)LSB case and (b) SSB case.	40
683	12	LSB case: (a) Locations along the estimated separated shear layer where velocity	
684		time signals are recorded. (b) Probability density function of streamwise velocity	
685		fluctuation normalised by the root-mean-square of the streamwise velocity fluctu-	
686		ation near the left abutment at all locations and (c) Probability density function of	
687		streamwise velocity fluctuation at all locations in the vicinity of the right abutment.	41
688	13	SSB case: (a) Locations along the estimated separated shear layer where velocity	
689		time signals are recorded. (b) Probability density function of streamwise velocity	
690		fluctuation normalised by the root-mean-square of the streamwise velocity fluctu-	
691		ation near the left abutment at all locations and (c) Probability density function of	
692		streamwise velocity fluctuation at all location in the vicinity of the right abutment. .	42
693	14	Quadrant analysis of the streamwise and spanwise velocity fluctuation normalised	
694		with u'_{RMS} for the LSB case.	43
695	15	Quadrant analysis of the streamwise and spanwise velocity fluctuation normalised	
696		with u'_{RMS} for the SSB case.	44
697	16	Power spectra of a streamwise and spanwise velocity fluctuation time series at lo-	
698		cation L7: (a) in log-log scale, (b) in semi-log scale, (c) out-of-plane vorticity con-	
699		tours in a horizontal plane near the water surface and (d) water surface represented	
700		by zero level set colour-coded by the water depth for the LSB case.	45
701	17	Power spectra of a streamwise and spanwise velocity fluctuation time series at lo-	
702		cation R5: (a) in log-log scale, (b) in semi-log scale, (c) out-of-plane vorticity	
703		contours in a horizontal plane near the water surface and (d) water surface repre-	
704		sented by zero level set colour-coded by the water depth for the LSB case.	46

705	18	Power spectra of a streamwise and spanwise velocity fluctuation time series at lo-	
706		cation L7: (a) in log-log scale, (b) in semi-log scale, (c) out-of-plane vorticity con-	
707		tours in a horizontal plane near the water surface and (d) water surface represented	
708		by zero level set colour-coded by the water depth for the SSB case.	47
709	19	Time series of the streamwise velocity at location L7 of the SSB case and stream-	
710		wise velocity contours at six selected instants in time labeled t_1 - t_6	48
711	20	Power spectra of a streamwise and spanwise velocity fluctuation time series at lo-	
712		cation R5: (a) in log-log scale, (b) in semi-log scale, (c) out-of-plane vorticity	
713		contours in a horizontal plane near the water surface and (d) water surface repre-	
714		sented by zero level set colour-coded by the water depth for the SSB case.	49

Fig. 1. Computational domains: (a) Long-setback abutment case, LSB, (b) Short-setback abutment case, SSB, (c) Cross-section including its dimensions.

Fig. 2. Definition sketch of the abutments and bridge area. The intersections between horizontal numbered lines (1-5) and vertical solid (LSB) and dashed (SSB) lines indicate the locations at which time-averaged streamwise velocity profiles (a)-(h) were measured experimentally.

Fig. 3. Computed and measured time-averaged streamwise velocity profiles at locations (a)-(h) (as described in Fig. 2) in cross-sections 2-4 of the LSB case. Experimental data (circles), coarse-mesh LES (dashed line), and fine-mesh LES (solid line).

Fig. 4. Computed and measured time-averaged streamwise velocity profiles at locations [a]-[h] (as described in Fig. 2) in cross-sections 2-4 of the SSB case. Experimental data (circles), coarse-mesh LES (dashed line), and fine-mesh LES (solid line).

Fig. 5. Computed (solid line) and measured (circles) profiles of the water surface for the LSB case at cross-section 2-4.

Fig. 6. Computed (solid line) and measured (circles) profiles of the water surface for the SSB case at cross-section 2-4.

Fig. 7. LES-predicted streamwise velocity contours in a selected horizontal plane: (a) instantaneous (b) time-averaged velocity for the LSB case.

Fig. 8. LES-predicted streamwise velocity contours in a selected horizontal plane: (a) instantaneous (b) time-averaged velocity for the SSB case.

Fig. 9. 2D streamlines near the abutment for (a) the LSB case and (b) the SSB case, 3D streamlines colour-coded with time-averaged streamwise velocity for (a) the LSB case and (b) the SSB case.

Fig. 10. Isosurfaces of the Q-criterion together with contours of the streamwise vorticity in selected cross-sections: (a) LSB case, (b) SSB case.

Fig. 11. Water surface deformation represented by zero level set and colour-coded by water depth for (a)LSB case and (b) SSB case.

Fig. 12. LSB case: (a) Locations along the estimated separated shear layer where velocity time signals are recorded. (b) Probability density function of streamwise velocity fluctuation normalised by the root-mean-square of the streamwise velocity fluctuation near the left abutment at all locations and (c) Probability density function of streamwise velocity fluctuation at all locations in the vicinity of the right abutment.

Fig. 13. SSB case: (a) Locations along the estimated separated shear layer where velocity time signals are recorded. (b) Probability density function of streamwise velocity fluctuation normalised by the root-mean-square of the streamwise velocity fluctuation near the left abutment at all locations and (c) Probability density function of streamwise velocity fluctuation at all location in the vicinity of the right abutment.

Fig. 14. Quadrant analysis of the streamwise and spanwise velocity fluctuation normalised with u'_{RMS} for the LSB case.

Fig. 15. Quadrant analysis of the streamwise and spanwise velocity fluctuation normalised with u'_{RMS} for the SSB case.

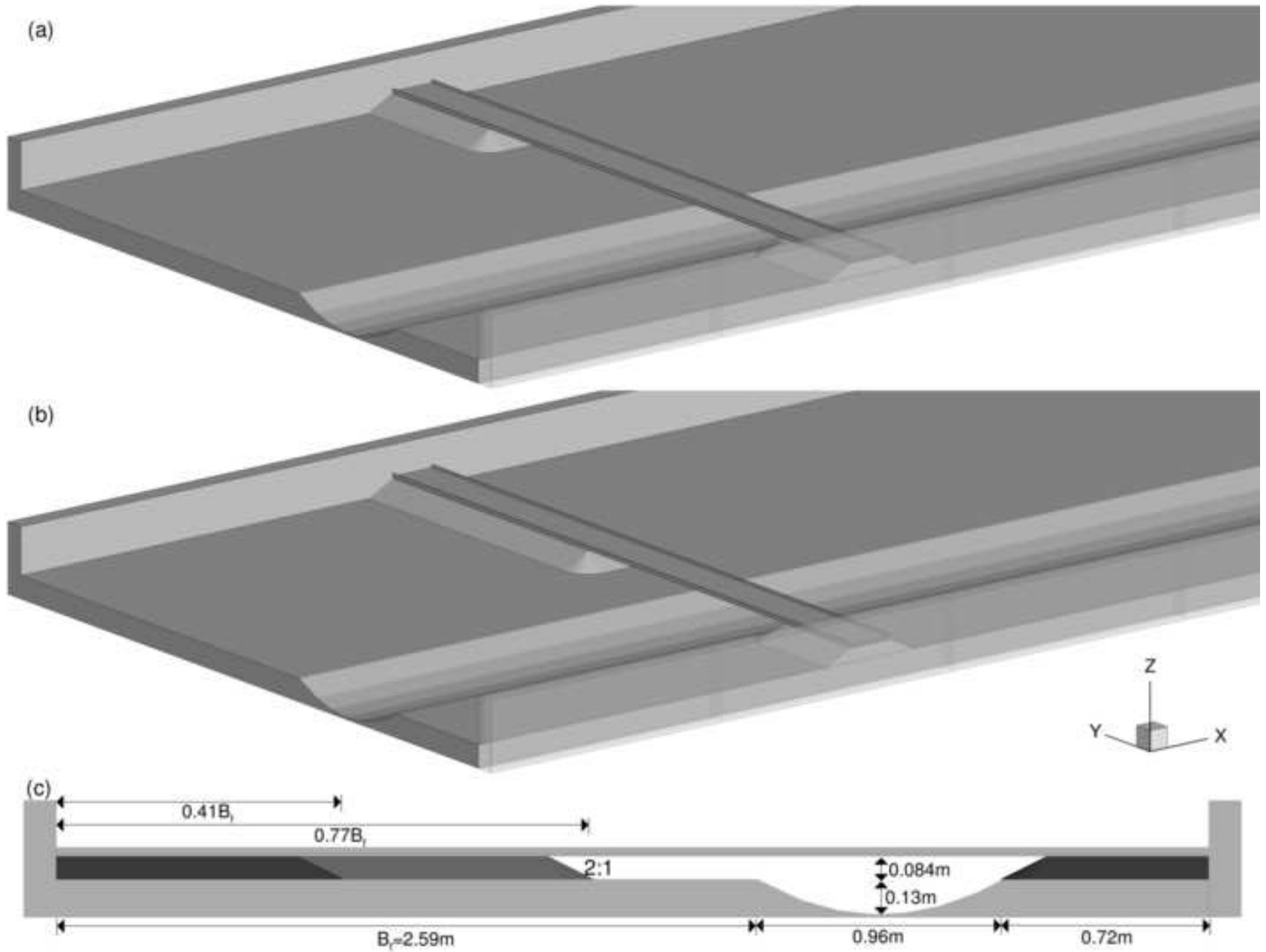
Fig. 16. Power spectra of a streamwise and spanwise velocity fluctuation time series at location L7: (a) in log-log scale, (b) in semi-log scale, (c) out-of-plane vorticity contours in a horizontal plane near the water surface and (d) water surface represented by zero level set colour-coded by the water depth for the LSB case.

Fig. 17. Power spectra of a streamwise and spanwise velocity fluctuation time series at location R5: (a) in log-log scale, (b) in semi-log scale, (c) out-of-plane vorticity contours in a horizontal plane near the water surface and (d) water surface represented by zero level set colour-coded by the water depth for the LSB case.

Fig. 18. Power spectra of a streamwise and spanwise velocity fluctuation time series at location L7: (a) in log-log scale, (b) in semi-log scale, (c) out-of-plane vorticity contours in a horizontal plane near the water surface and (d) water surface represented by zero level set colour-coded by the water depth for the SSB case.

Fig. 19. Time series of the streamwise velocity at location L7 of the SSB case and streamwise velocity contours at six selected instants in time labeled t_1 - t_6 .

Fig. 20. Power spectra of a streamwise and spanwise velocity fluctuation time series at location R5: (a) in log-log scale, (b) in semi-log scale, (c) out-of-plane vorticity contours in a horizontal plane near the water surface and (d) water surface represented by zero level set colour-coded by the water depth for the SSB case.



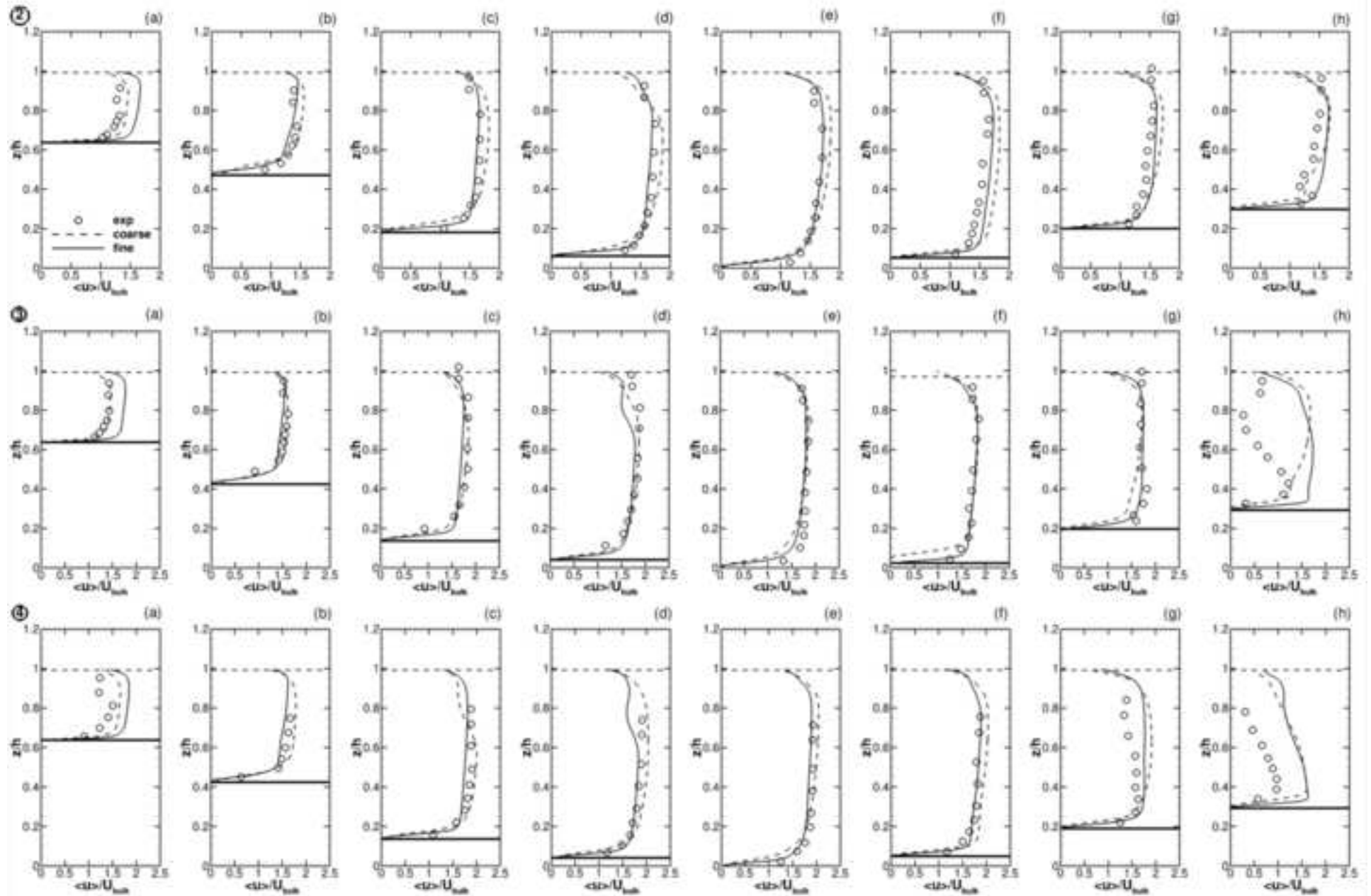


Figure 4

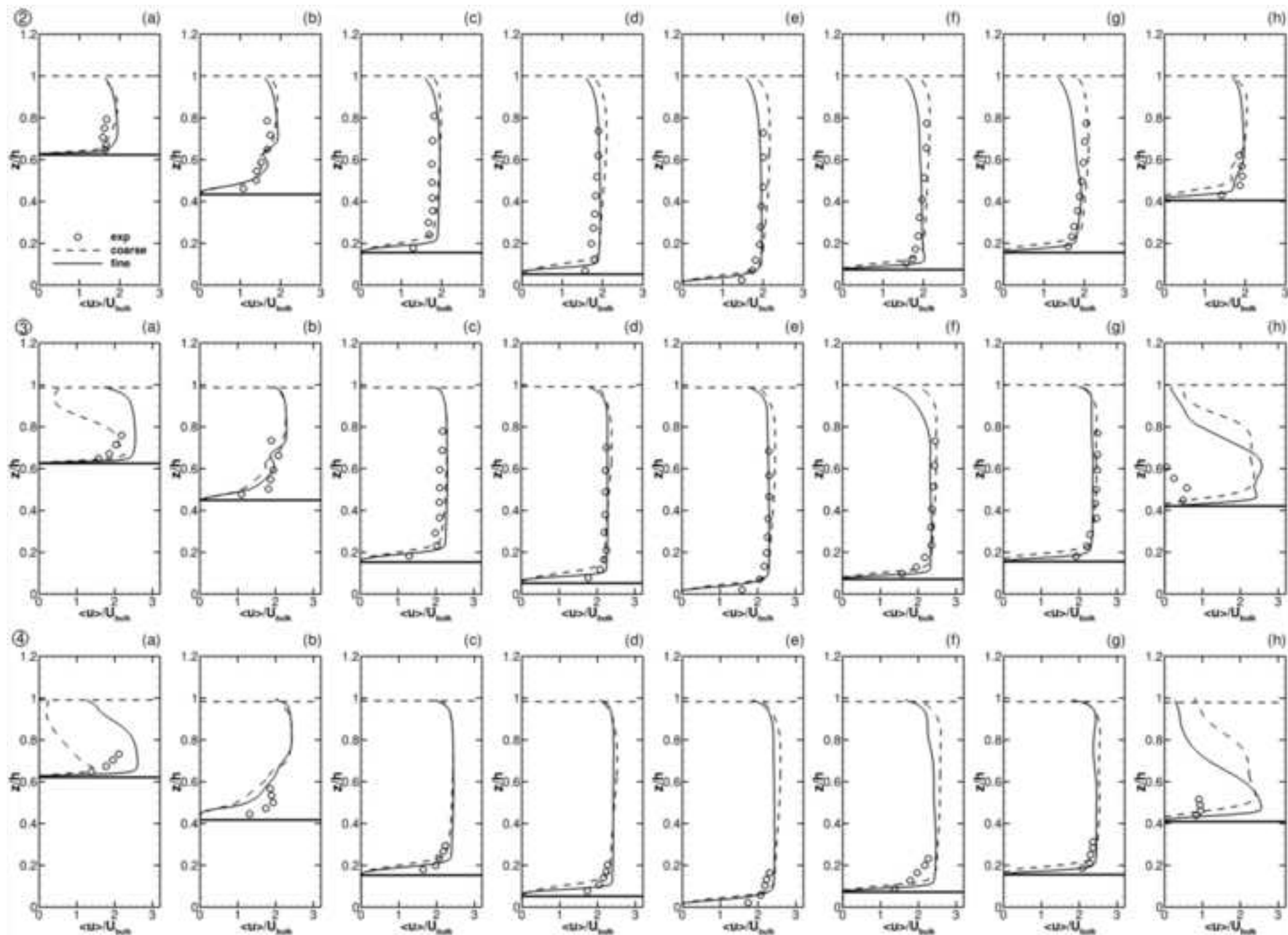
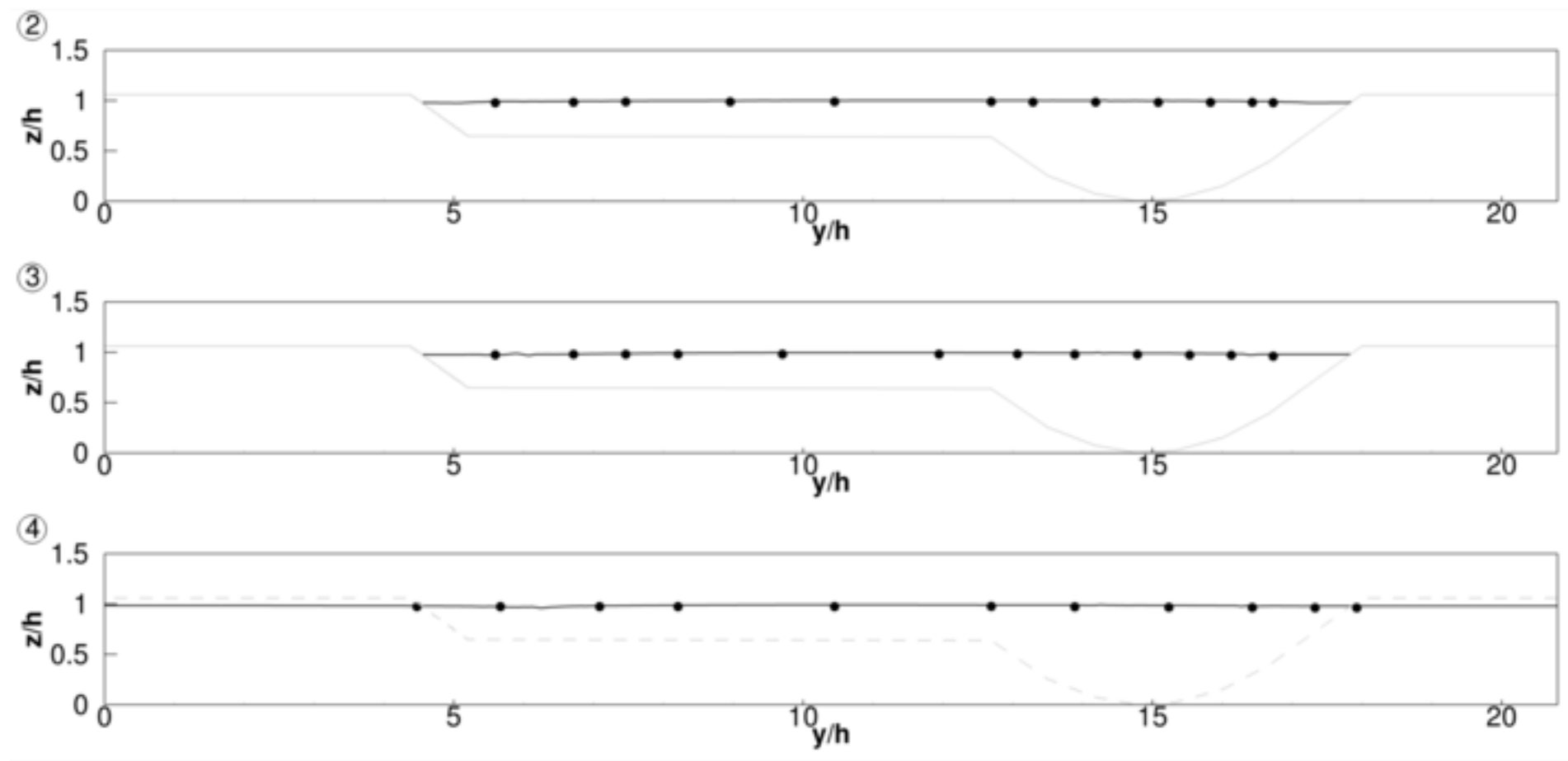
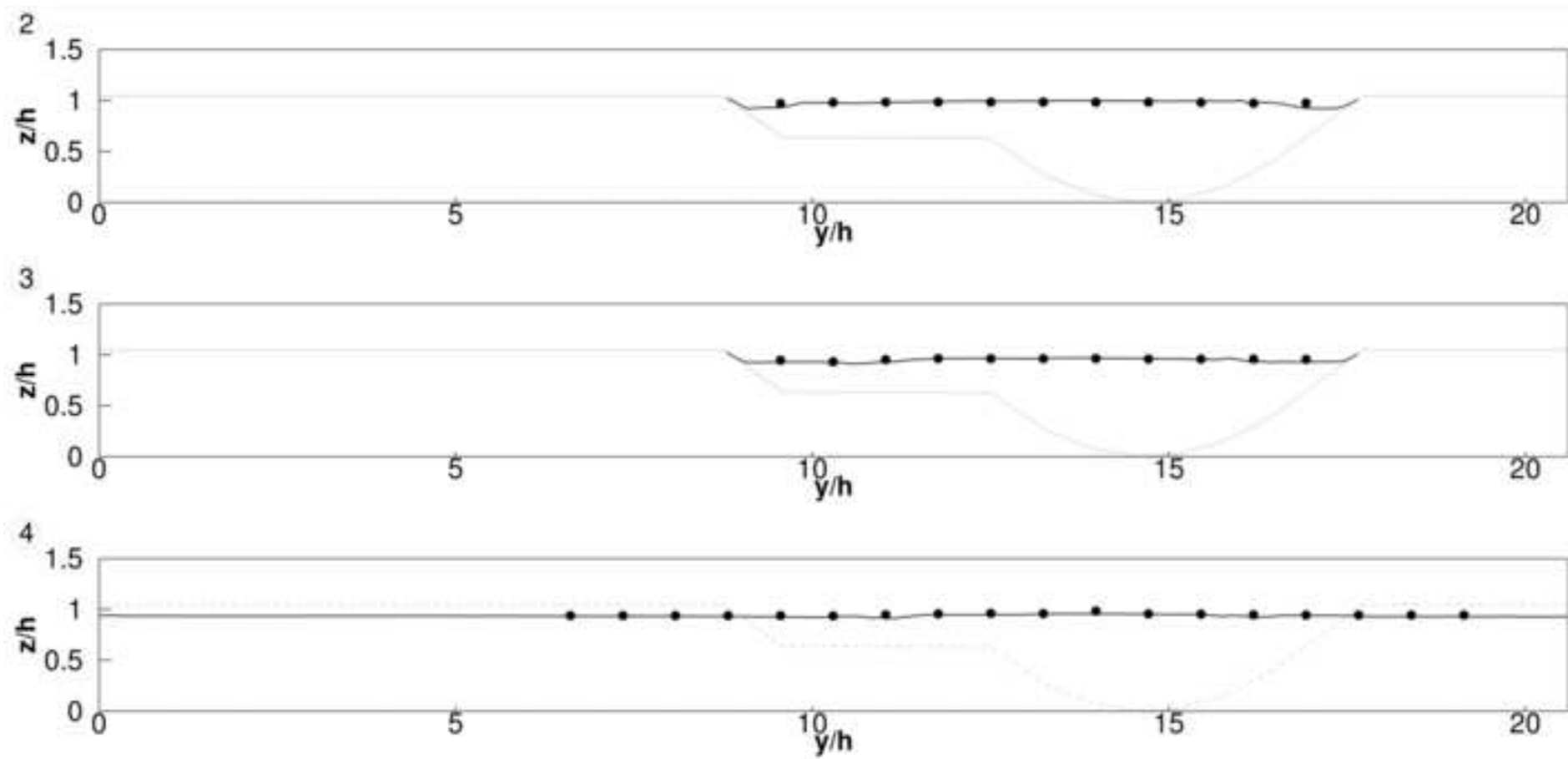
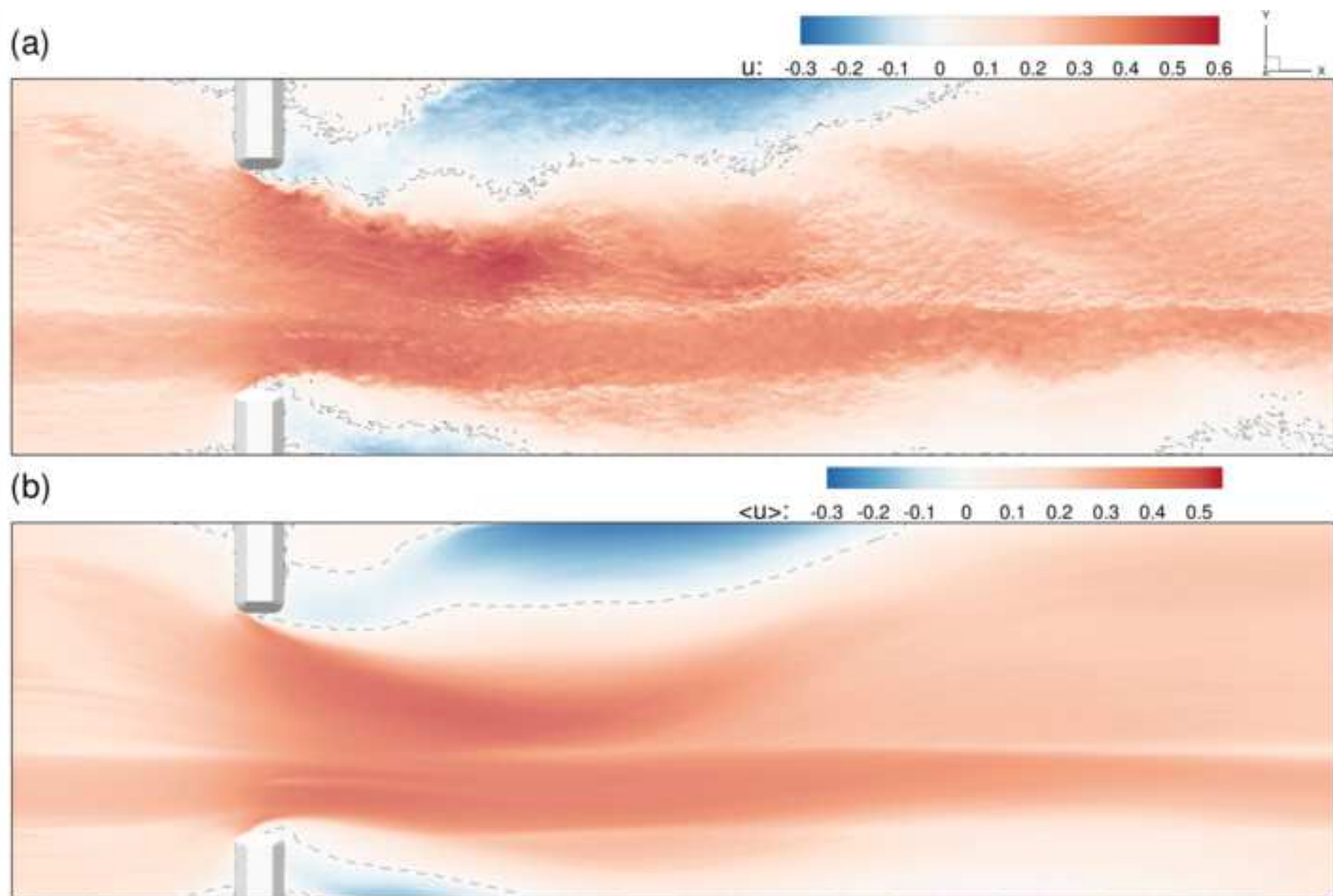
[Click here to access/download;Figure;fig4.tiff](#)

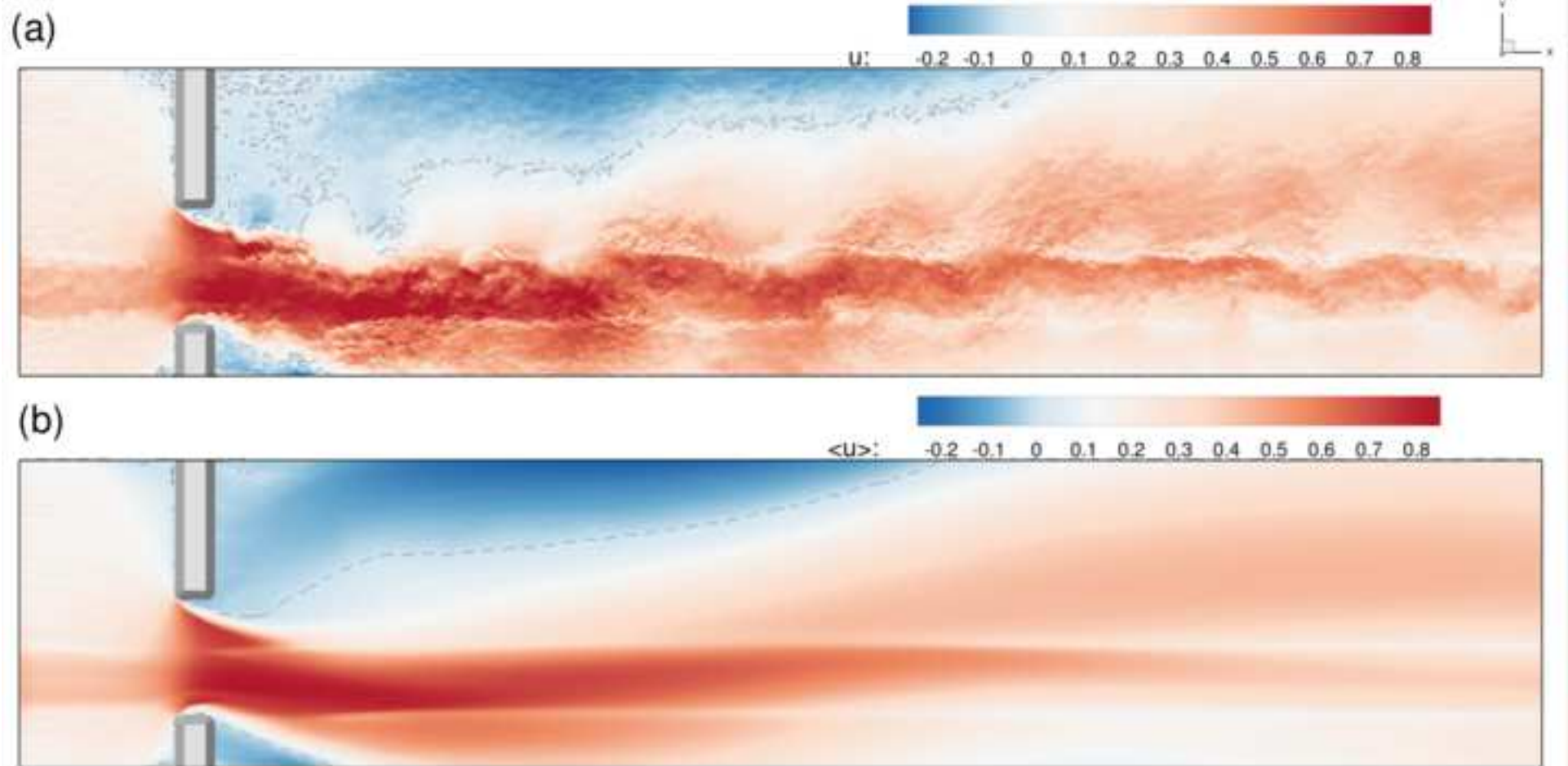
Figure 5

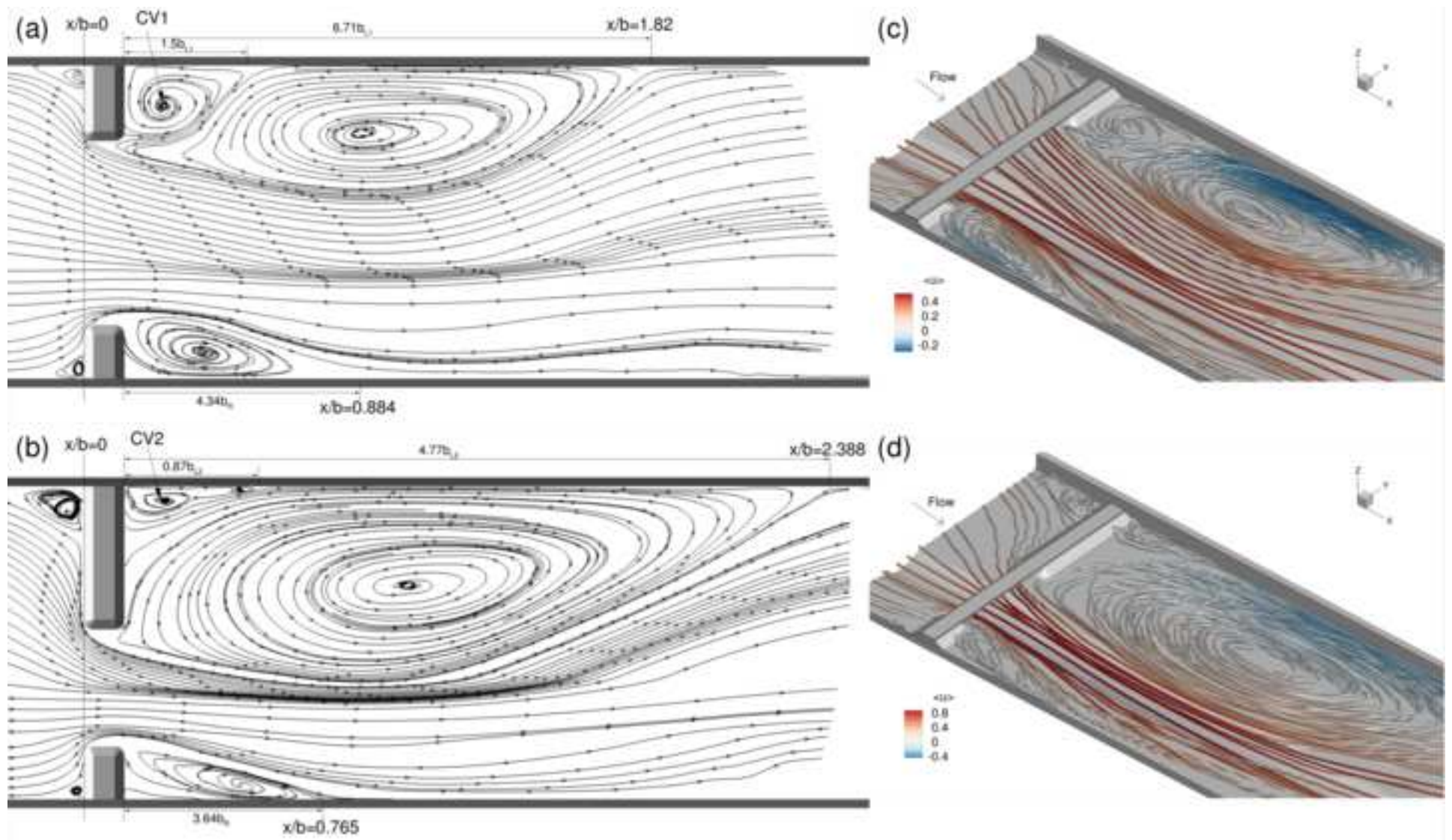
[Click here to access/download;Figure;fig5.tiff](#)

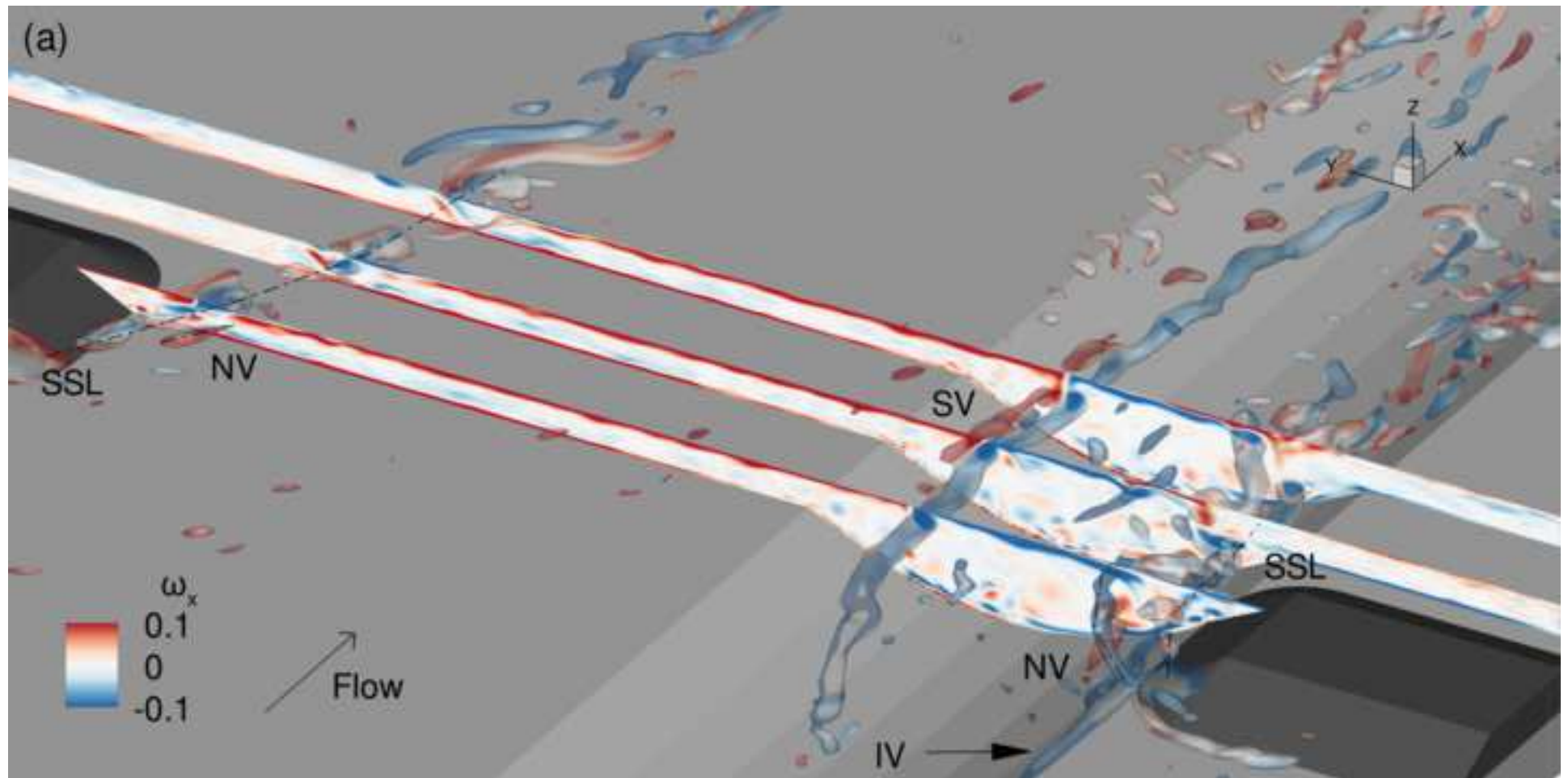


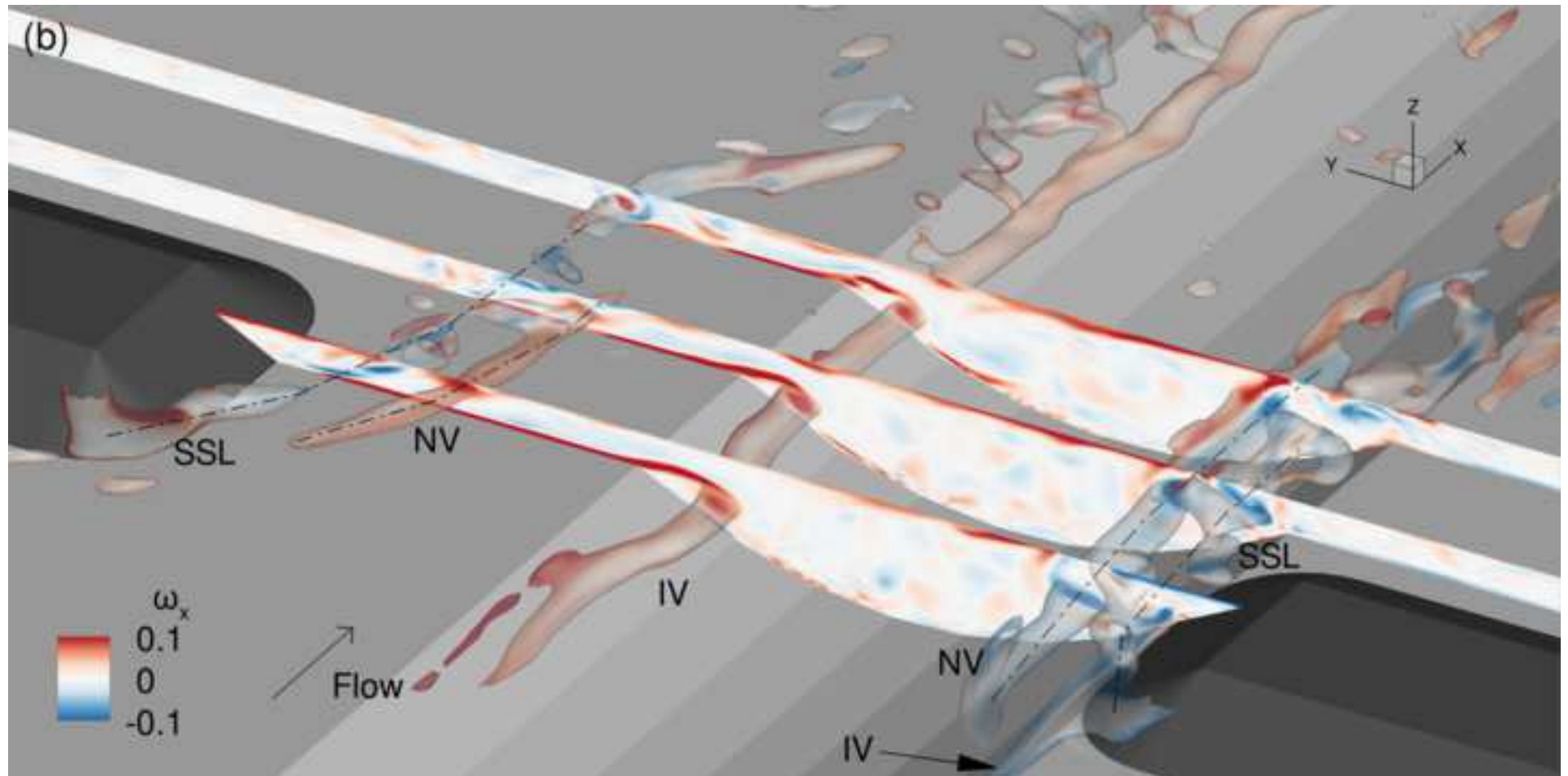


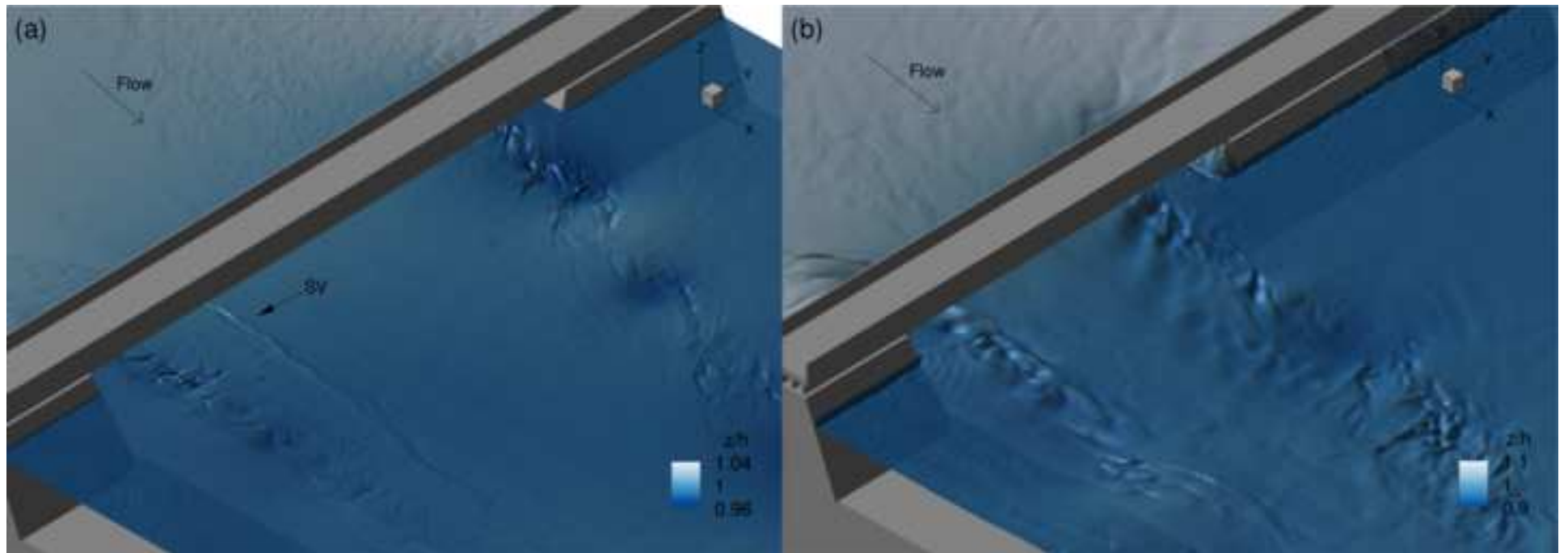


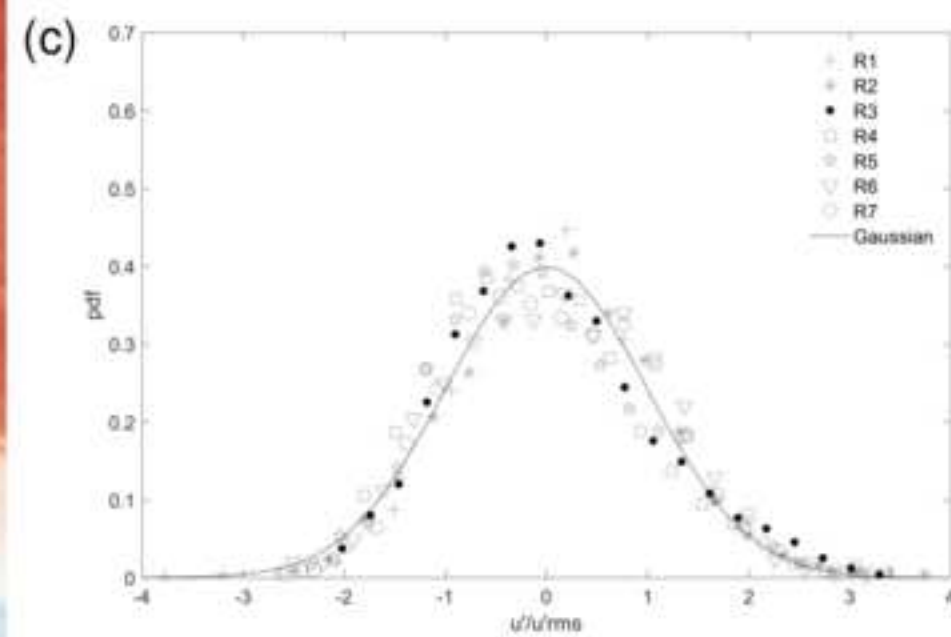
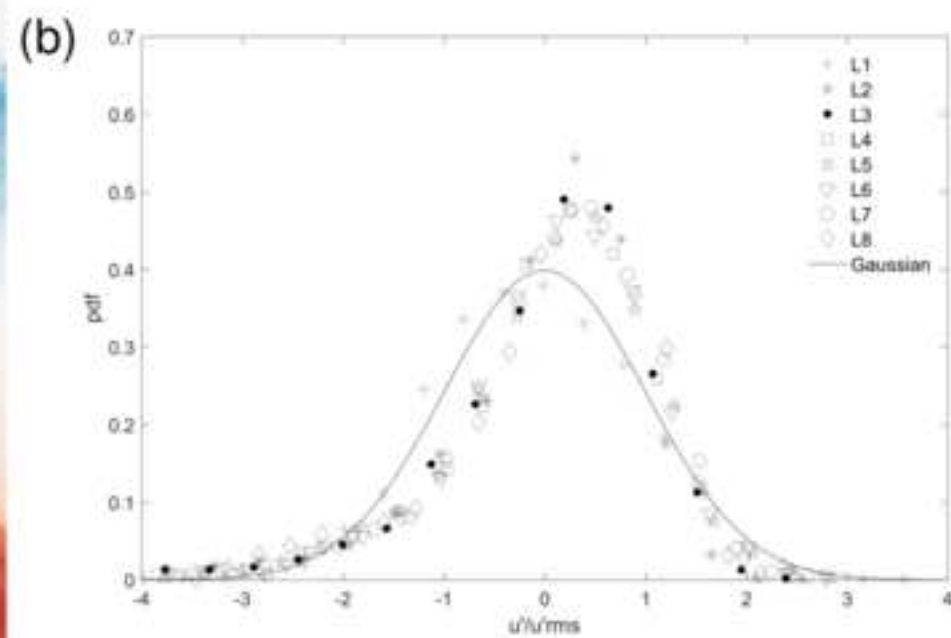












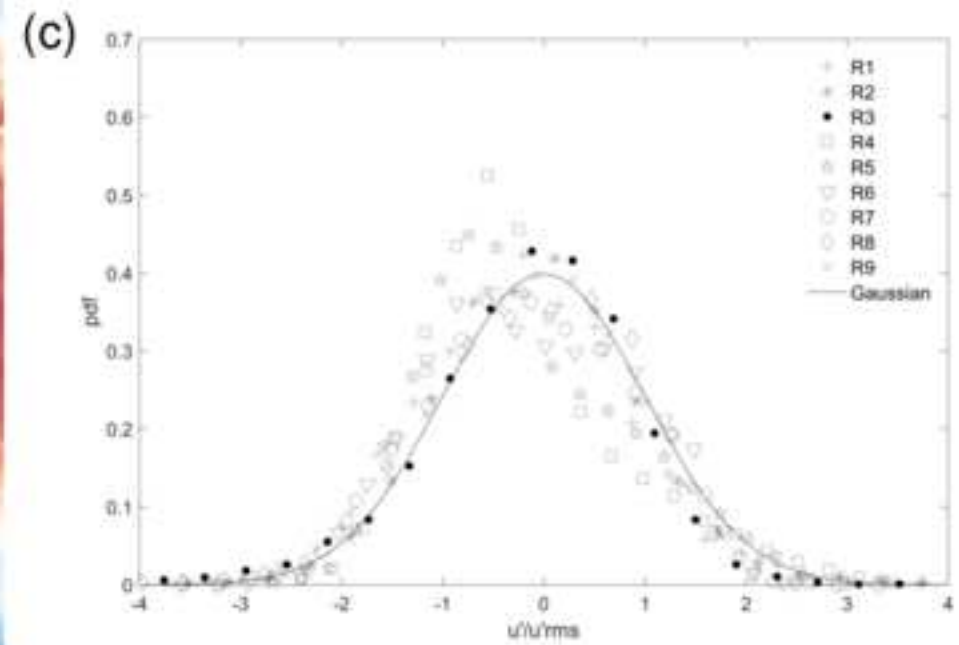
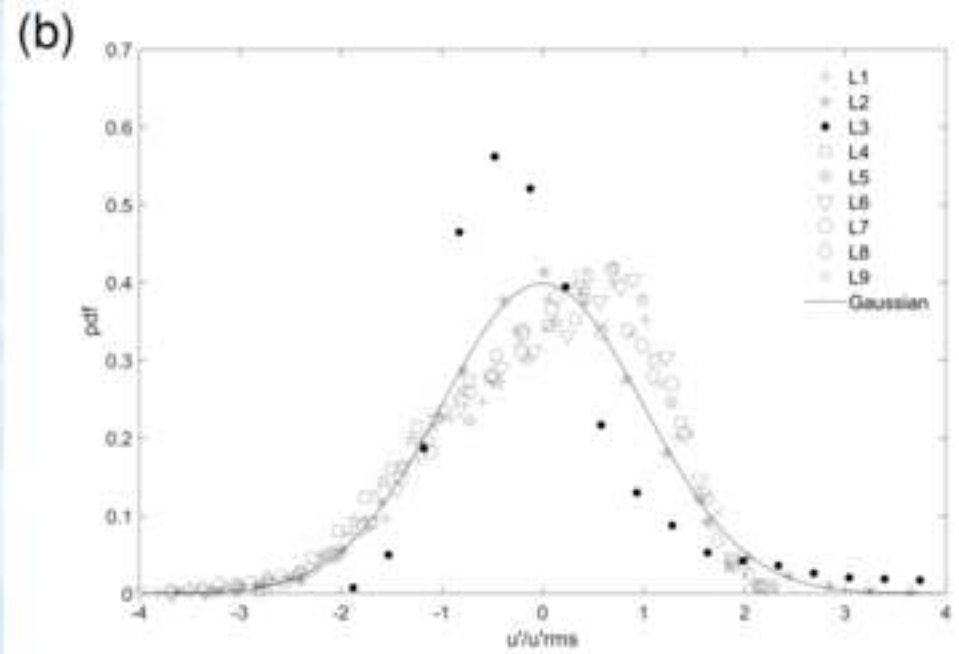
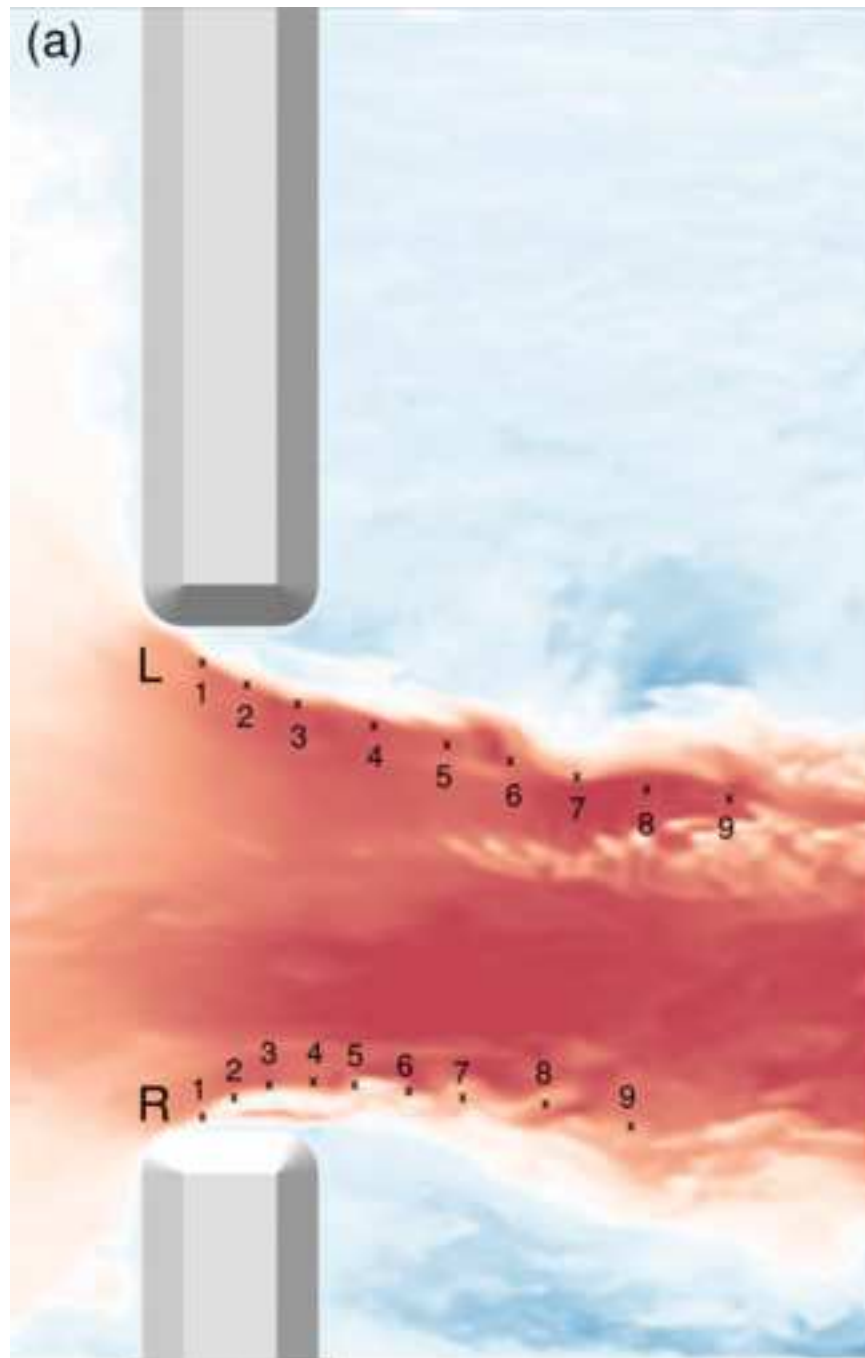


Figure 14

[Click here to access/download;Figure;fig14.tiff](#)

